

1 **Magnetotelluric multiscale 3-D inversion reveals**  
2 **crustal and upper mantle structure beneath the**  
3 **Hangai and Gobi-Altai region in Mongolia**

4 J.S. Käuffl<sup>1</sup>, A.V. Grayver<sup>1</sup>, M.J. Comeau<sup>2</sup>, A.V. Kuvshinov<sup>1</sup>, M. Becken<sup>2</sup>,  
J. Kamm<sup>2,3</sup>, E. Batmagnai<sup>1</sup>, S. Demberel<sup>4</sup>

<sup>1</sup>*Institute of Geophysics, Department of Earth Sciences, ETH Zürich, Switzerland*

<sup>2</sup>*Institut für Geophysik, WWU Münster, Germany*

<sup>3</sup>*Geological Survey of Finland, Espoo, Finland*

<sup>4</sup>*Institute of Astronomy and Geophysics, Mongolian Academy of Sciences, Ulaanbaatar, Mongolia*

5 28 October 2019

This is a non-peer reviewed manuscript (Preprint) submitted to EarthArXiv.

6 This manuscript was also submitted to Geophysical Journal International and is currently  
undergoing review.

**7 Summary**

8 Central Mongolia is a prominent region of intracontinental surface deformation and in-  
9 traplate volcanism. To study these processes, which are poorly understood, we collected  
10 magnetotelluric data in the Hangai and Gobi-Altai region in central Mongolia and derived  
11 the first three-dimensional (3-D) resistivity model of the crustal and upper mantle structure  
12 in this region.

13 The geological and tectonic history of this region is complex, resulting in features over  
14 a wide range of spatial scales, which that are coupled through a variety of geodynamic  
15 processes. Many Earth properties that are critical for the understanding of these processes,  
16 such as temperature as well as fluid and melt properties, affect the electrical conductivity in  
17 the subsurface. 3-D imaging using magnetotellurics can resolve the distribution of electrical  
18 conductivity within the Earth at scales ranging from tens of metres to hundreds of kilometres,  
19 thereby providing constraints on possible geodynamic scenarios. We present an approach  
20 to survey design, data acquisition, and inversion that aims to bridge various spatial scales  
21 while keeping the required field work and computational cost of the subsequent 3-D inversion  
22 feasible.

23 Magnetotelluric transfer functions were estimated for a  $650 \times 400 \text{ km}^2$  grid, which in-  
24 cluded measurements on an array with regular  $50 \times 50 \text{ km}^2$  spacing and along several profiles  
25 with a denser 5-15 km spacing. The use of telluric-only data loggers on these profiles allowed  
26 for an efficient data acquisition with a high spatial resolution. A 3-D finite element forward  
27 modelling and inversion code was used to obtain the resistivity model. Locally refined un-  
28 structured hexahedral meshes allow for a multi-scale model parametrization and accurate  
29 topography representation. The inversion process was carried out over four stages, whereby  
30 the result from each stage was used as input for the following stage that included a finer  
31 model parametrization and/or additional data (i.e. more stations, wider frequency range).

32 The final model reveals a detailed resistivity structure and fits the observed data well,  
33 across all periods and site locations, offering new insights into the subsurface structure  
34 of central Mongolia. A prominent feature is a large low-resistivity zone detected in the

35 upper mantle. This feature suggests a non-uniform lithosphere-asthenosphere boundary that  
36 contains localized upwellings that shallow to a depth of 70 km, consistent with previous  
37 studies. The 3-D model reveals the complex geometry of the feature, which appears rooted  
38 below the Eastern Hangai Dome with a second smaller feature slightly south of the Hangai  
39 Dome.

40 Within the highly resistive upper crust, several conductive anomalies are observed. These  
41 may be explained by late Cenozoic volcanic zones and modern geothermal areas, which  
42 appear linked to mantle structures, as well as by major fault systems, which mark terrane  
43 boundaries and mineralized zones. Well resolved, heterogeneous low-resistivity zones that  
44 permeate the lower crust may be explained by fluid-rich domains.

45 **Key words:** Magnetotellurics, Inverse theory, Numerical modelling, Electrical proper-  
46 ties, Asia, Structure of the Earth

## 47 1 INTRODUCTION

48 Located deep in the continental interior, far away from plate boundaries, central Mongolia  
49 is a region of active intracontinental deformation (Calais et al. 2003; Walker et al. 2007,  
50 2008) and young Cenozoic volcanism (e.g. Barry et al. 2003; Ancuta et al. 2018). With  
51 the stable Siberian Craton to the North, central Mongolia occupies the transition zone  
52 between the North-South compressional regime of the India-Asia collision and an eastward  
53 motion (Calais et al. 2003). This transition zone is dominated by the Hangai Dome, a low  
54 relief, intracontinental plateau elevated up to 2 km above the regional average (Cunningham  
55 2001). It is bounded by large seismically active strike slip faults, which experienced large  
56 (Magnitude > 8, Rizza et al. 2015) intracontinental earthquakes in the last century (Walker  
57 et al. 2007). Additionally, dispersed, low-volume, intraplate volcanism has occurred during  
58 the last 35 Ma throughout central Mongolia (Barry et al. 2003; Hunt et al. 2012; Ancuta  
59 et al. 2018).

60 The cause of the volcanism and the mechanism for the Hangai Dome uplift remain enig-  
61 matic. In particular, the link between intracontinental uplift and intraplate volcanism is an

open topic of research. In the case of central Mongolia, some authors argue for contemporaneous processes (e.g. Cunningham 2001; Sahagian et al. 2016), whereas others suggest that the uplift might have predated the volcanic activity (McDannell et al. 2018).

Previous seismic and gravity studies of the region found a low velocity/low density anomaly in the upper mantle below the Hangai Dome confined to depths of 70 – 150 km (Priestley et al. 2006; Tiberi et al. 2008), and a low shear-wave velocity anomaly that possibly extends to a depth of more than 410 km (Chen et al. 2015). Across central Mongolia, a thick crust (45–55 km) was determined by seismic studies, with the thickest part directly below the Hangai Dome (Petit et al. 2008). Seismic studies also observed a shallow (60–80 km) lithosphere-asthenosphere-boundary (LAB) below the Hangai Dome (Priestley et al. 2006; Petit et al. 2008). Geochemical analysis of erupted lavas and mantle xenoliths estimates the melting source at depths of 70 to 150 km (Ionov 2002; Barry et al. 2003; Hunt et al. 2012), in good agreement with a shallow asthenosphere and with the observed low velocity/low density anomalies.

This combined evidence is inconsistent with an earlier explanation for the intraplate volcanism: a deep-rooted mantle plume (Windley & Allen 1993). More recent explanations for the volcanism and uplift include crust-mantle interactions such as lithospheric thinning (due to delamination, convective removal, or edge-driven convection) or asthenospheric flow and dynamic topography (see e.g. Ancuta et al. 2018). However, a comprehensive explanation is still missing, partly due to a lack of detailed images of the subsurface in this region. To obtain this information, a magnetotelluric survey was conducted in the Hangai and Gobi-Altai region from 2016 to 2018.

Magnetotellurics (MT) images the electrical resistivity of the subsurface, which is primarily controlled by the quantity and composition of fluids, the porosity, and the temperature (e.g. Unsworth & Rondenay 2013; Manning 2018). Low-resistive domains in the crust or upper mantle can therefore often be associated with the presence of inter-connected saline fluids or partial melts. Because fluid (and melt) networks lower the bulk resistivity and can have a mechanical weakening effect on rocks (Liu & Hasterok 2016), resistivity images al-



low for inferences on the rheology of the lithosphere. Comprehensive geodynamic scenarios should therefore ultimately be able to account for resistivity images from MT.

In the past, three-dimensional (3-D) inversion of MT data has been used to successfully image the subsurface from the crust into the upper mantle. On a local scale, MT provided models of shallow volcanic and geothermal systems with small extents of approximately 10 km (e.g. Heise et al. 2007; Bertrand et al. 2012; Muñoz 2014; Hill et al. 2015; Peacock et al. 2016; Usui et al. 2016; Samrock et al. 2018). At regional scales, MT is commonly used to image crustal and lithospheric structures (e.g. Khoza et al. 2013; Tietze & Ritter 2013; Nieuwenhuis et al. 2014; Cherevatova et al. 2015; Robertson et al. 2017; Xu et al. 2019) and in recent years, models obtained by inverting continental scale surveys have appeared, including the USArray, AusLAMP, and SinoProbe projects (e.g. Meqbel et al. 2014; Yang et al. 2015; Robertson et al. 2016; Dong et al. 2016; Murphy & Egbert 2017). However, the resistivity anomalies related to geological and geodynamic processes caused by crust-mantle interactions, such as the intracontinental deformation and intraplate volcanism in Mongolia, can be observed over the entire range of spatial scales covered in these surveys. Hence, this was the motivation to design a MT survey and develop a 3-D inversion scheme that can consistently embrace and bridge multiple spatial scales.

In practice, any survey design is often limited by the cost of data acquisition and the required logistical effort. Because a uniform, dense grid of sites can be prohibitively expensive to collect, an attractive alternative is complementing a coarser, large-scale grid of sites with more densely spaced sites in regions of primary interest. Data acquisition can further be optimized with the Telluric-Magnetotelluric (T-MT) method (Hermance & Thayer 1975), whereby the magnetic field is recorded only at a subset of locations (Iliceto & Santarato 1986; Yungul 1977; García & Jones 2005; Melosh et al. 2010; Campányà et al. 2014). From a methodological perspective, handling T-MT data requires only modest modifications to the data processing and inversion tools to take full advantage of simultaneously recording arrays (Egbert 2002). For the three-dimensional interpretation of MT data collected at an observation grid of highly variable spacing, one needs an inversion strategy that provides

118 sufficient flexibility in parametrizing the subsurface. This allows varying lateral and vertical  
 119 resolution lengths to be appropriately accounted for without using an excessive number of  
 120 unknown model parameters, which would impose additional computational constraints and  
 121 increase non-uniqueness.

122 In this paper we focus on the methodological side of the problem and present an approach  
 123 on how to bridge the different spatial scales in 3-D MT inversions, applied to the data  
 124 collected in the Hangai and Gobi-Altai mountains in central Mongolia. Conductive anomalies  
 125 are described, and potential explanations, in the context of the regional geodynamics and  
 126 geology, are offered. Earlier results by Comeau et al. (2018c), based on a 2-D model from a  
 127 subset of the data, are expanded upon with new insights from the 3-D resistivity model.

## 128 2 DATA

### 129 2.1 The magnetotelluric method

130 The MT method is a geophysical technique used to probe the conductivity structure of  
 131 the Earth by using natural electromagnetic (EM) field variations (Rikitake 1948; Tikhonov  
 132 1950; Cagniard 1953). The Earth's response to external excitation is described by frequency-  
 133 dependent transfer functions (TF), which carry information about the electrical conductivity  
 134 distribution. We work with the magnetotelluric impedance tensor  $\mathbf{Z}$ , which links horizontal  
 135 electric and magnetic fields as:

$$\vec{E}_h(\omega, \vec{r}_l) = \mathbf{Z}(\omega, \vec{r}_l) \vec{H}_h(\omega, \vec{r}_l). \quad (1)$$

136 Here,  $\omega$  is the angular frequency.  $\vec{E}_h(\omega, \vec{r}_l) = (E_x, E_y)$  and  $\vec{H}_h(\omega, \vec{r}_l) = (H_x, H_y)$  are the  
 137 Fourier transforms of the horizontal components of the electric (E-) and magnetic (H-) fields  
 138 at the location  $\vec{r}_l$ . Henceforth, the frequency dependence is implied and will be omitted for  
 139 simplicity. H- and E-fields act as the input and output of the linear system described by the  
 140 impedance

$$\mathbf{Z}(\vec{r}_l) = \begin{pmatrix} Z_{xx}(\vec{r}_l) & Z_{xy}(\vec{r}_l) \\ Z_{yx}(\vec{r}_l) & Z_{yy}(\vec{r}_l) \end{pmatrix}, \quad (2)$$

141 which is a second-order frequency dependent, complex-valued tensor. It carries the infor-  
 142 mation about the 3-D electrical conductivity distribution  $\sigma$  in the earth. Instead of the  
 143 conductivity, its inverse, the resistivity ( $\rho = \sigma^{-1}$ ) can be used interchangeably. For each of  
 144 the four tensor elements we can calculate the phase

$$\phi_{ij}(\vec{r}_l) = \tan^{-1}(Z_{ij}(\vec{r}_l)) \quad \text{with } i, j \in \{x, y\} \quad (3)$$

145 and apparent resistivity

$$\rho_{a,ij}(\vec{r}_l) = \frac{|Z_{ij}(\vec{r}_l)|^2}{\omega\mu_0}, \quad (4)$$

146 where  $\mu_0$  is the magnetic permeability of vacuum.

147 Conventionally, electric and magnetic fields are recorded at the same location  $\vec{r}_l$ . The  
 148 T-MT method (Hermance & Thayer 1975) introduces an inter-site impedance,  $\mathbf{Z}_i$ , defined  
 149 as

$$\vec{E}_h(\vec{r}_l) = \mathbf{Z}_i(\vec{r}_l, \vec{r}_b) \vec{H}_h(\vec{r}_b), \quad (5)$$

150 whereby  $\mathbf{Z}_i$  is calculated with the E-field measured at the location  $\vec{r}_l$  and the H-field mea-  
 151 sured at the location  $\vec{r}_b$  (denoted as base site). The different  $\vec{r}_l$  locations of E-field and B-field  
 152 measurements ( $\vec{r}_l$  and  $\vec{r}_b$ ) are taken into account for the forward modelling and inversion  
 153 of intersite impedances (see Sections 3.1 and 3.2 below). Recently, Comeau et al. (2018c)  
 154 inverted a single profile of MT data across Mongolia and showed that using  $\mathbf{Z}_i$  does not  
 155 compromise resolution and leads to reliable subsurface images. In fact, this approach can  
 156 further help in suppressing local noise (Egbert 2002; Campanyà et al. 2014).

## 157 2.2 Data acquisition

158 During three field surveys in the years 2016 to 2018, data was collected on a  $650 \times 400$  km<sup>2</sup>  
 159 grid (see Fig. 1 and Table 1 for abbreviations of geographic features). The survey covers  
 160 the Hangai Mountains, a part of the Gobi-Altai mountain range, the Valley of Lakes, and  
 161 surrounding areas. For the inversion model presented below, we use transfer functions from  
 162 272 unique locations with 97 sites laid out on a quasi-uniform grid with 50 km spacing and  
 163 175 sites along four profiles (P2, P3, P4, and P6 in Fig. 1) with a spacing of 5 to 15 km.

---

AS:	Asthenosphere
BF:	Bogd fault
BUF:	Bulnay fault
CV:	Chuluut volcanic zone
EHC:	East Hangai conductor
GAC:	Gobi-Altai conductor
GAF:	Gobi-Altai fault
HB:	Hangai block
LAB:	Lithosphere-Asthenosphere boundary
NHC:	North Hangai conductor
SHC:	South Hangai conductor
SHF:	South Hangai fault
TV:	Tariat volcanic zone
TGT:	Tsenkher geothermal area
VL:	Valley of Lakes
VLR:	Valley of Lakes resistor
WHC:	West Hangai conductor

---

**Table 1.** Table of abbreviations used throughout the text and in figures.

164 Additional sites are located in the Tariat volcanic field (TV, Comeau et al. 2018a) and the  
 165 Tsenkher geothermal area (TGT).

166 We employed two types of instruments: broadband (B) and telluric-only (T). Generally,  
 167 B-instruments were used for the grid sites, while T-instruments were installed on the pro-  
 168 files. For some of the sites we had to deviate from this scheme due to data quality issues  
 169 and instrument availability during the measurement campaign. All instruments recorded  
 170 the horizontal electric field (60 m dipole length with either silver-chloride or lead-chloride  
 171 electrodes). B-sites additionally recorded all three components of the magnetic field. At B-  
 172 locations, Metronix ADU-07e and SPAM Mk4 data loggers with Metronix induction coils  
 173 (MFS-06 and MFS-10) were used. Recording was done for three to five days with a sampling  
 174 frequency of 512 Hz. Additional long period instruments (Geomag Fluxgate and EarthData  
 175 data loggers) were installed at 14 locations along profiles P2 and P4. Recording time was  
 176 between 10 and 32 days with a sampling frequency of 2 Hz. The telluric instruments were

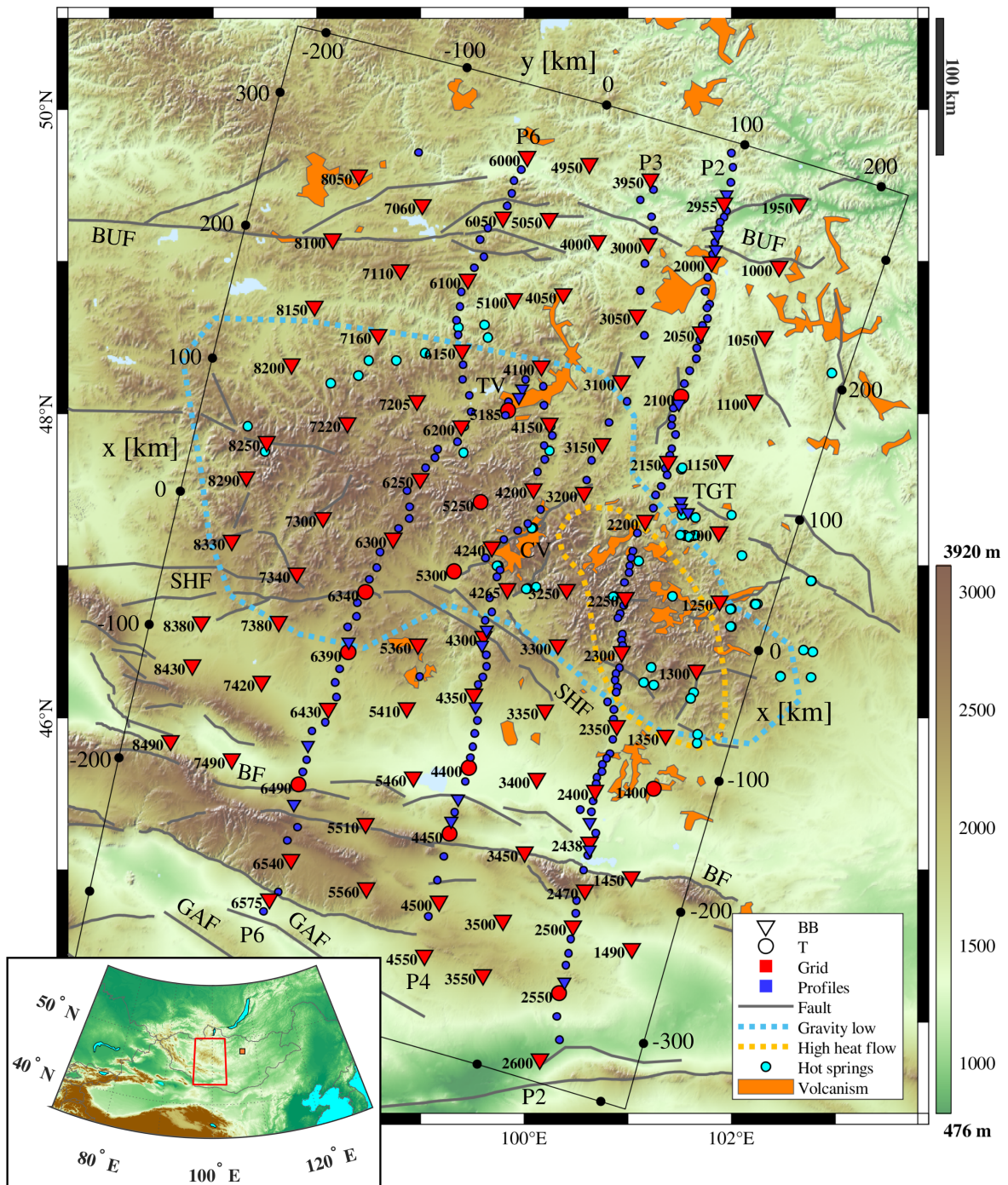


**Figure 1.** Topographic map with installed sites in central Mongolia. The location in central Asia is indicated in the smaller inset in the lower left. See Table 1 for abbreviations. The symbol indicates the type of instrument used. Red color indicates the grid sites and blue color the others. The grid sites are indicated with their numeric designation. Grey lines mark major fault systems (Walker et al. 2008; Styron 2018), the dotted blue line indicates the -250 mGal Bouguer anomaly (Tiberi et al. 2008), the dotted orange line indicates the 90 mW/m<sup>2</sup> high heat flow anomaly, light blue circles mark hot spring locations (Oyuntsetseg et al. 2015; Ganbat & Demberel 2010), and the orange patches designate Cenozoic volcanic provinces (Ancuta et al. 2018). The black frame around the survey area indicates the rotated local cartesian coordinate system used for the 3-D inversion.

177 designed by the University of Münster for fast and easy deployment, thus allowing for effi-  
 178 cient data collection with dense site spacing. They recorded with a sampling frequency of  
 179 512 Hz for a duration of twelve hours to three days.

### 180 2.3 Transfer functions

181 Impedance tensors were estimated with a robust processing scheme, using the M-estimator  
 182 (Egbert & Booker 1986) and a minimal covariance determinant method (Rousseeuw 1984;  
 183 Platz & Weckmann 2019) to improve long period TF when only a few time windows are  
 184 available (Harpering 2018). To maximise the quality and period range of TF, processing  
 185 parameters (such as time window selection, bi-coherence threshold values, single site or  
 186 remote referencing, base site selection for inter-site impedances) were chosen individually  
 187 for each site. After processing, we obtained a set of 272 TF of high quality in the period  
 188 range from 0.0078 s to 3000 s at most sites with periods going up to 8000 s and 24000 s  
 189 for some broad-band and long-period sites, respectively. Fig. 2 shows a representative set of  
 190 transfer functions at four locations.

191 Overall, the data is affected by galvanic distortions. For instance, 4150BL in Fig. 2  
 192 exhibits a static shift effect for  $T > 0.5$  s (large differences between  $\rho_{xy}$  and  $\rho_{yx}$  but with  
 193 similarly-shaped curves, as well as similar  $\phi_{xy}$  and  $\phi_{yx}$ ). Berdichevsky et al. (1980) suggested  
 194 that an regional 1-D impedance can be obtained with the geometric mean of the determinant  
 195 of  $\mathbf{Z}$ . In this paper, we use the sum of the squared impedance elements (SSQ-impedance)

$$Z_{ssq}(\vec{r}_l) = \sqrt{\frac{Z_{xx}(\vec{r}_l)^2 + Z_{xy}(\vec{r}_l)^2 + Z_{yx}(\vec{r}_l)^2 + Z_{yy}(\vec{r}_l)^2}{2}} \quad (6)$$

196 for each location  $\vec{r}_l$ . Compared to the impedance determinant,  $Z_{ssq}$  is less affected by a  
 197 downward bias due to distortion (Rung-Arunwan et al. 2016). The regional 1-D impedance,

$$\bar{Z}_{1-D} = \sqrt[N]{\prod_{l=1}^N Z_{ssq}(\vec{r}_l)}, \quad (7)$$

198 is calculated with the geometric average, where  $N$  denotes the total count of locations used.

199 The apparent resistivities and phases obtained from the SSQ-impedances for the grid sites  
 200 north and south of the South Hangai Fault (SHF) are shown in Fig. 3a) for periods  $T > 1$  s.

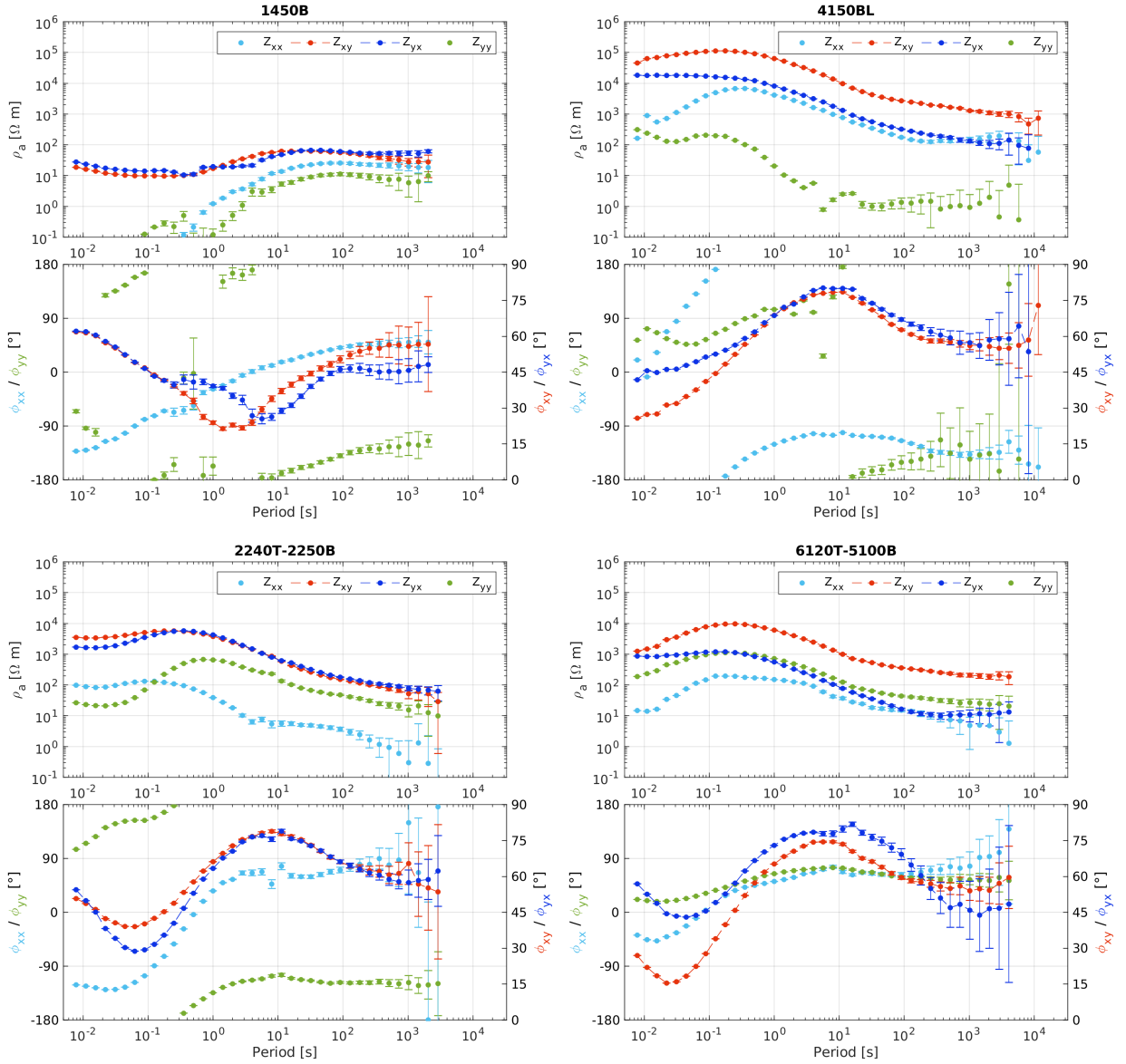


**Figure 2.** Apparent resistivity and phase curves at four representative sites. The off-diagonal phases ( $\phi_{xy}$  and  $\phi_{yx}$ ) are shifted to the first quadrant for better visibility. 1450B is a broadband site, 4150BL is a broadband and long-period site, 2240T and 6120T are telluric sites with their respective base sites given in the plot titles.

201 Generally, we see in Fig. 3a) that  $Z_{ssq}$  from northern sites (see e.g. 4150BL, 2240T, and 6120T  
 202 in Fig. 2) exhibit much less spatial variability compared to the sites south of the SHF (see e.g.  
 203 1450B in Fig. 2 as well as 2350BL and 4350BL in Fig. 5). Apparent resistivities for northern  
 204 sites vary over two orders of magnitude, most likely due to galvanic distortions, but the shape  
 205 of the  $\rho_a$  curves and the phase shows smaller variability, especially for periods  $T > 10$  s.



206 We conclude that the 1-D impedance calculated from averaged northern SSQ-impedances  
 207 provides a reasonable representation of the regional 1-D conductivity structure. Southern  
 208 sites, on the other hand, show a large variability in both  $\rho_a$  and  $\phi$  curves over the entire  
 209 period range, indicating a substantially inhomogeneous regional conductivity distribution.  
 210 As a result, the southern regional 1-D impedance is likely not representative of a regional  
 211 conductivity structure.

212 Further, Fig. 3b shows the real part of the C-response,

$$C = -\frac{\bar{Z}_{1-D}}{i\omega\mu_0}, \quad (8)$$

213 calculated for both regional 1-D impedances. It represents the depth of the “center of mass”  
 214 of induced currents for a given period (Weidelt 1972) and can be used as a proxy for the  
 215 penetration depth. Starting with a penetration depth of 4-15 km at 1 s, the penetration  
 216 depth increases to 200 km at the period of 4096 s.

217 We performed a dimensionality analysis by calculating the phase tensor strike angle  $\theta$   
 218 and the normalized skew angle  $\Psi$  (Booker 2014). The polar histograms of  $\theta$  in Fig. 4 reveals  
 219 a preferred strike direction for periods  $T > 10$  s, namely  $15^\circ \pm 90^\circ$  (clockwise from magnetic  
 220 North). With a normalized skew angle of  $|\Psi| > 6^\circ$  over a wide period range at the majority  
 221 of the sites (see the supplementary material, Sec. S1), the collected data shows a significant  
 222 influence of 3-D effects (Booker 2014). Thus a 3-D inversion is indeed indispensable to  
 223 retrieve all information from the dataset.

224 As was previously shown by Tietze & Ritter (2013), when a predominant geological strike  
 225 direction exists, it is advantageous to rotate the impedance tensor even for 3-D inversion,  
 226 thereby improving inversion convergence and reducing modelling errors. Therefore, we ro-  
 227 tated the impedance tensors by  $15^\circ$  counter-clockwise, thus aligning the principal axes not  
 228 only with the strike directions but also the profile directions. An additional benefit of the  
 229 rotation is the correction of out of quadrant off-diagonal phases, that can be observed at  
 230 some of the sites. This is shown in Fig. 5 for two sites, 2350BL and 4350BL. For both sites  
 231  $\rho_{xy} > \rho_{yx}$ , indicating East-West oriented low resistivity anomalies. A phase tensor analysis



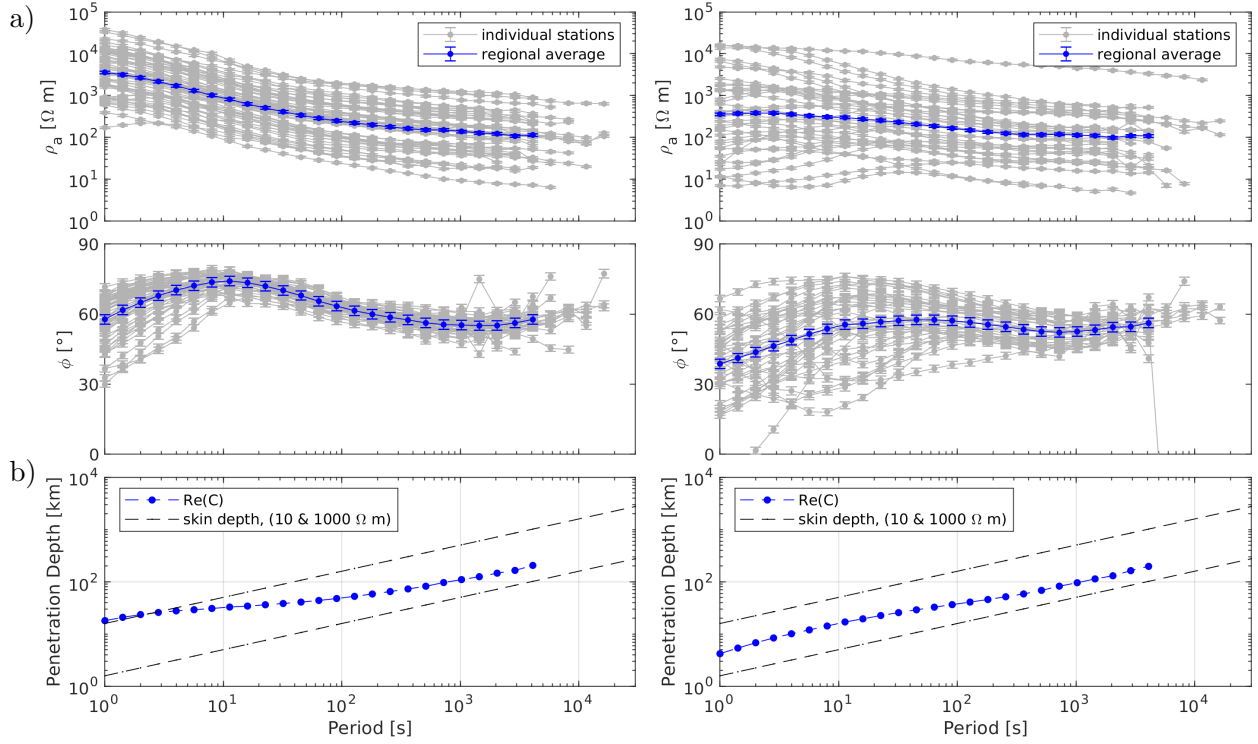


**Figure 3.** SSQ-impedances and penetration depths estimated from grid site data north (left) and south (right) of the SHF (see Fig. 1). a)  $\rho_a$  and  $\phi$  calculated from the SSQ-impedance of each individual site (grey) and from the regional 1-D impedance (Eq. 7; blue). b) The real part of the C-response for both regional 1-D averages, a measure for the penetration depth, together with the skin depths for a homogeneous half space of 10 and 1000 Ωm.

232 of these sites reveals strong 3-D influences with a normalized skew angle of  $|\Psi| > 6^\circ$  in the  
 233 period range of 0.1–10 s, indicating that shallow (less than 10 km) 3-D anomalies are most  
 234 likely the cause of these out of quadrant phases. After rotating the impedance tensor by  $15^\circ$   
 235 counter-clockwise from magnetic North, phases remain in their respective quadrants for the  
 236 entire period range.

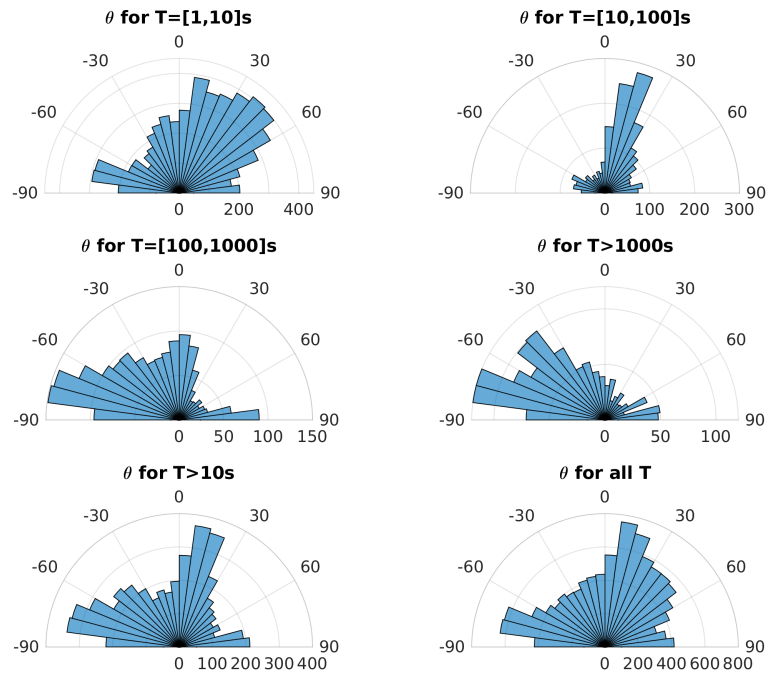


**Figure 4.** Polar histograms of the phase tensor strike angle  $\theta$  (clockwise from magnetic North) for different period bands. From 10 s to 100 s a clear strike direction of  $15^\circ$  can be seen, whereas longer periods show a strike of  $-75^\circ$ .

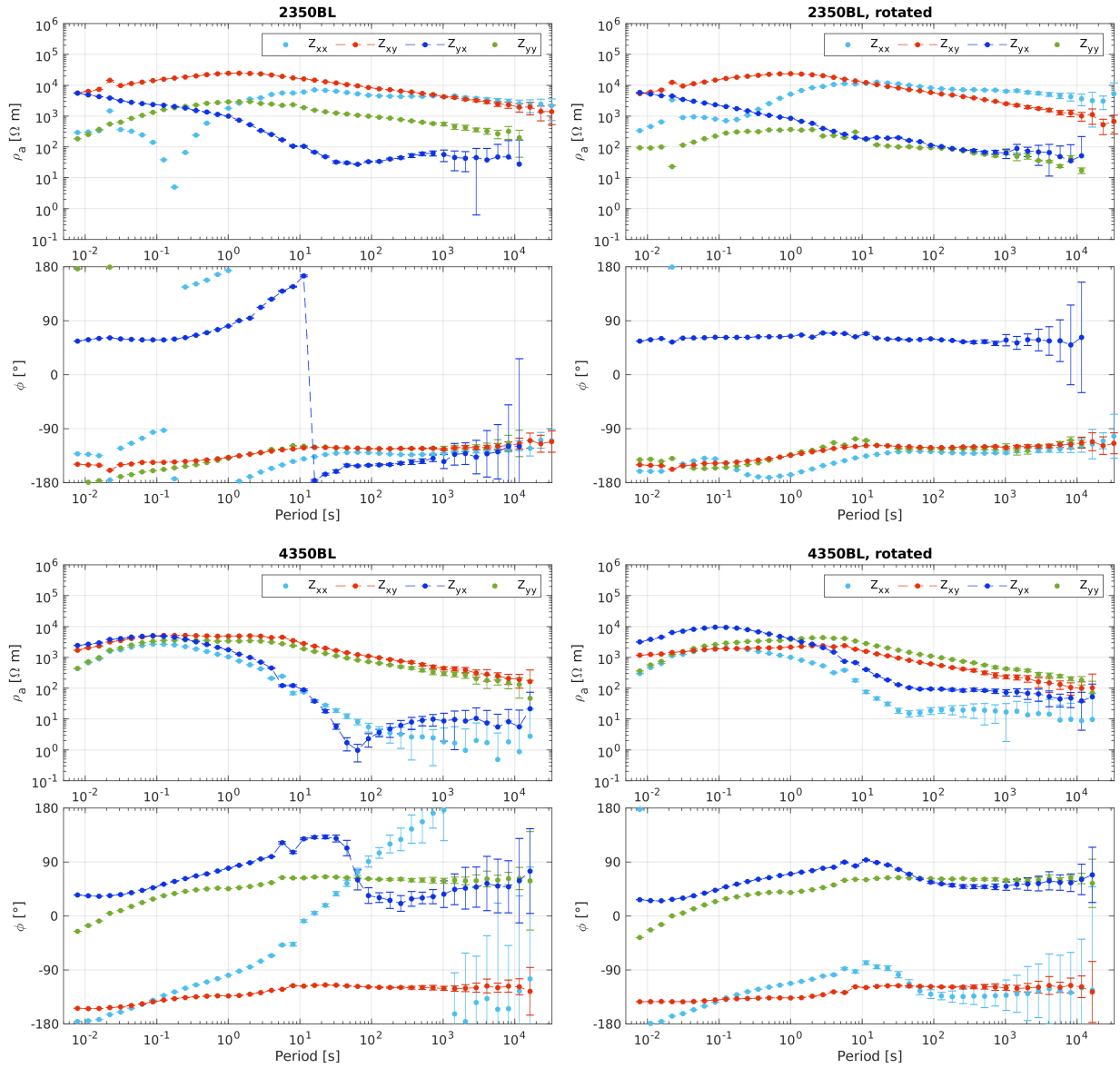


**Figure 5.** Sounding curves for the sites 4350BL and 2350BL, left: coordinate system oriented along magnetic North, right: rotated coordinate system ( $15^\circ$  counterclockwise from magnetic North). After rotation, previously out of quadrant phases remain in their respective quadrants over the entire period range.

### 3 METHODOLOGY

Owing to the wide frequency range of MT source signals ( $10^{-4}$  to  $\approx 10^5$  s), together with the typical electrical resistivity range of the Earth (0.1 to  $10^5$   $\Omega\text{m}$ ), the inversion of MT data can efficiently resolve electrical resistivity variations in a wide range of spatial scales from tens of metres to hundreds of kilometres. Here, we aim at combining MT data from a regional-scale array and locally dense profile sites, encompassing a period range over five decades. We address this challenge by introducing a 3-D multi-scale inversion scheme. Our approach is outlined below.

#### 3.1 Forward modelling

Electromagnetic fields in a 3-D medium are calculated by solving the following equation

$$\nabla \times (\mu_0^{-1} \nabla \times \vec{E}) + i\omega\sigma\vec{E} = 0 \quad \text{in } \Omega. \quad (9)$$

Here,  $\Omega \subseteq R^3$  is the modelling domain,  $\vec{E}$  the electric field vector and  $\sigma$  the electrical conductivity. Further, the inhomogeneous Dirichlet boundary conditions,

$$\vec{E} = \vec{E}_0 \quad \text{on } \partial\Omega, \quad (10)$$

are applied, where  $\vec{E}_0$  results from the solution of 2-D Maxwell's equations on the boundaries.

The magnetic field  $\vec{H}$  is obtained by virtue of Faraday's law. Solutions for two orthogonal source polarisations are computed to be able to derive the full impedance tensor.

The 3-D finite element code GoFEM (Grayver & Kolev 2015) was used to discretize Eq. (9) and find a numerical solution. It is based on the finite-element library deal.II (Alzetta et al. 2018) and uses PETSc (Balay et al. 2018) with METIS (Karypis & Kumar 1999) for distributed linear algebra and mesh partitioning, respectively. The resulting system of linear equations was solved with a parallel version of the iterative FGMRES solver and auxiliary-space multigrid preconditioner as described in detail by Grayver & Kolev (2015). To improve accuracy of the numerical solutions and to discretize topography accurately, we used locally refined non-conforming hexahedral meshes, as described in Section 3.3.

### 3.2 Inversion

To obtain the electrical conductivity distribution that explains the measured data we solve a non-linear inverse problem (e.g. Dmitriev et al. 1976; Aster et al. 2018) by minimising the objective function

$$\Phi(\mathbf{m}) = \frac{1}{2}\Phi_d(\mathbf{d}, \mathbf{m}) + \frac{\alpha}{2}\Phi_m(\mathbf{m}), \quad (11)$$

which consists of a data term  $\Phi_d$  and a model term  $\Phi_m$ , balanced by the regularization parameter  $\alpha$ .  $\mathbf{m}$  is a vector of the unknown model parameters (i.e. the electrical conductivity) and  $\mathbf{d}$  the data vector, containing the TF. For this study we used the real and imaginary parts of either the regional 1-D impedance (Eq. 7, for a 1-D inversion) or all four impedance tensor components (Eq. 2, for a 3-D inversion). Given that the phase tensors indicate strong 3-D effects in parts of the data, 2-D/3-D tensor decompositions (e.g. Groom & Bailey 1989; Bahr 1991; Smith 1997) are not applicable. Therefore, no attempt was made to correct for galvanic distortion.

The data term

$$\Phi_d(\mathbf{m}, \mathbf{d}) = \|(f(\mathbf{m}) - \mathbf{d})\|_{\mathbf{C}_d^{-1}}^2, \quad (12)$$

contains the difference between the observed and the modelled TFs, which are obtained from the forward modelling operator  $f(\mathbf{m})$  given a model  $\mathbf{m}$ . The data is weighted by the the data covariances  $\mathbf{C}_d$ , given here by a diagonal matrix containing the data variance  $\delta Z^2$ .

Because of strong galvanic distortions, a relative error  $e$  was applied row-wise to the absolute of  $\mathbf{Z}$  at each period, giving data variances

$$\delta Z_{jx}^2 = \delta Z_{jy}^2 = (e \cdot \max(|Z_{jx}|, |Z_{jy}|))^2 \quad \text{with } j \in \{x, y\}. \quad (13)$$

To prevent imbalance between grid and profile sites, we found that an error  $e = 0.03$  for the grid and  $e = 0.05$  for the profiles allows us to achieve a uniform fit for all sites. Thereby, TF at the profile sites are slightly down-weighted in comparison to TF from the grid sites.

The model or regularization term

$$\Phi_m(\mathbf{m}) = \|\mathbf{R}(\mathbf{m})\|^2 \quad (14)$$

is given by the roughness operator  $R(\vec{m})$ , aimed to stabilize the ill-posed and generally non-unique inverse problem (Tikhonov 1963). No reference model is used in the regularization term. Thereby, the roughness of the model (characterized by the conductivity jumps across adjacent cells) is minimized.

GoFEM uses the Gauss-Newton method to minimize the functional in Eq. (11) (Grayver 2015). A unit step length for the model update is used. While this can lead to an increase in  $\Phi$ , it usually allows the inversion to escape a local minimum.

The regularization parameter

$$\alpha = \gamma \frac{\|\mathbf{J}^T \mathbf{C}_d^{-1} \mathbf{J}\|_2}{\|\mathbf{R}\|_2} \quad (15)$$

is determined for each iteration step by the ratio of the  $L_2$ -norms of the weighted approximate Hessian  $\mathbf{J}^T \mathbf{C}_d^{-1} \mathbf{J}$  and the regularization matrix  $\mathbf{R}$ .  $\mathbf{J}$  denotes the Jacobian of  $f(\mathbf{m})$ . The scaling factor  $\gamma \in (0, 1]$  is a user-determined parameter. We adopted a cooling regularization by gradually decreasing the regularization strength through smaller  $\gamma$ . In practice, this approach facilitates the recovery of the dominating large-scale conductivity variations followed by smaller structures later during the inversion process.

### 3.3 Model discretization

The modelling domain  $\Omega$  is discretized using hexahedral elements. To ensure numerical accuracy and to decrease the ambiguity of the non-unique problem, we use locally refined meshes. As outlined by Käüfl et al. (2018), an initially coarse mesh is locally refined within the area of interest and then transformed to conform to the topography.

The mesh used in this study has a size of  $4000 \times 4000 \times 3000 \text{ km}^3$  and consists of 6800 cells initially. The subsequent refinements were guided by the penetration depth inferred from the C-responses (Fig. 3b). After two refinements at the air-ground interface, three refinements in the central area of interest, and three refinements around site locations, the mesh consists of 215000 cells. Within the survey area, cell diameters range from 4.7 km close to the MT sites to 19 km in the upper mantle down to a depth of 200 km. At greater depths and outside the

307 survey area, cells increase gradually towards the domain boundary. Finally, the meshes are  
308 adjusted to the topography (elevation data provided by NASA JPL 2013) and cells in the  
309 air are assigned a resistivity of  $10^9 \Omega\text{m}$ . The resulting mesh is shown in Fig. 6a. A second  
310 finer mesh is obtained by further refinement, resulting in 321000 cells with a minimal cell  
311 diameter of 2.4 km near sites (Fig. 6b). This represents our inverse model parametrization.

312 As is shown by Joshi et al. (2004) and Grayver (2015), it may be advantageous to decou-  
313 ple forward/adjoint and inverse model parametrizations. Specifically, we use an additional  
314 refinement step in a 5 km radius around site locations for forward and adjoint solutions in  
315 order to better represent local topography and increase numerical accuracy for higher fre-  
316 quencies. A coarser mesh for the targeted parameter (that is, electrical conductivity) reduces  
317 computational cost and decrease ambiguity, thereby making the problem less ill-posed. Note  
318 that due to hierarchical relation between both forward/adjoint and inverse grids, we avoid  
319 any interpolation and simply assign conductivity from the coarser inverse grid cells to refined  
320 forward/adjoint grid cells.

321 Following the arguments from Section 2.3, we perform the inversion in a local Cartesian  
322 coordinate system with x- and y-axes rotated  $15^\circ$  clockwise from North and East respectively.  
323 The z-axis points downward. The origin corresponds to the center of the survey grid at  
324  $47^\circ\text{N}$ ,  $99.5^\circ\text{E}$  (sea level). All geographic coordinates are transformed into the modelling  
325 domain by referencing their UTM coordinates (zone 47, WGS84 reference ellipsoid) to  $47^\circ\text{N}$ ,  
326  $99.5^\circ\text{E}$  followed by a rotation around the origin. The resulting cartesian coordinate system  
327 is indicated in Fig. 1.

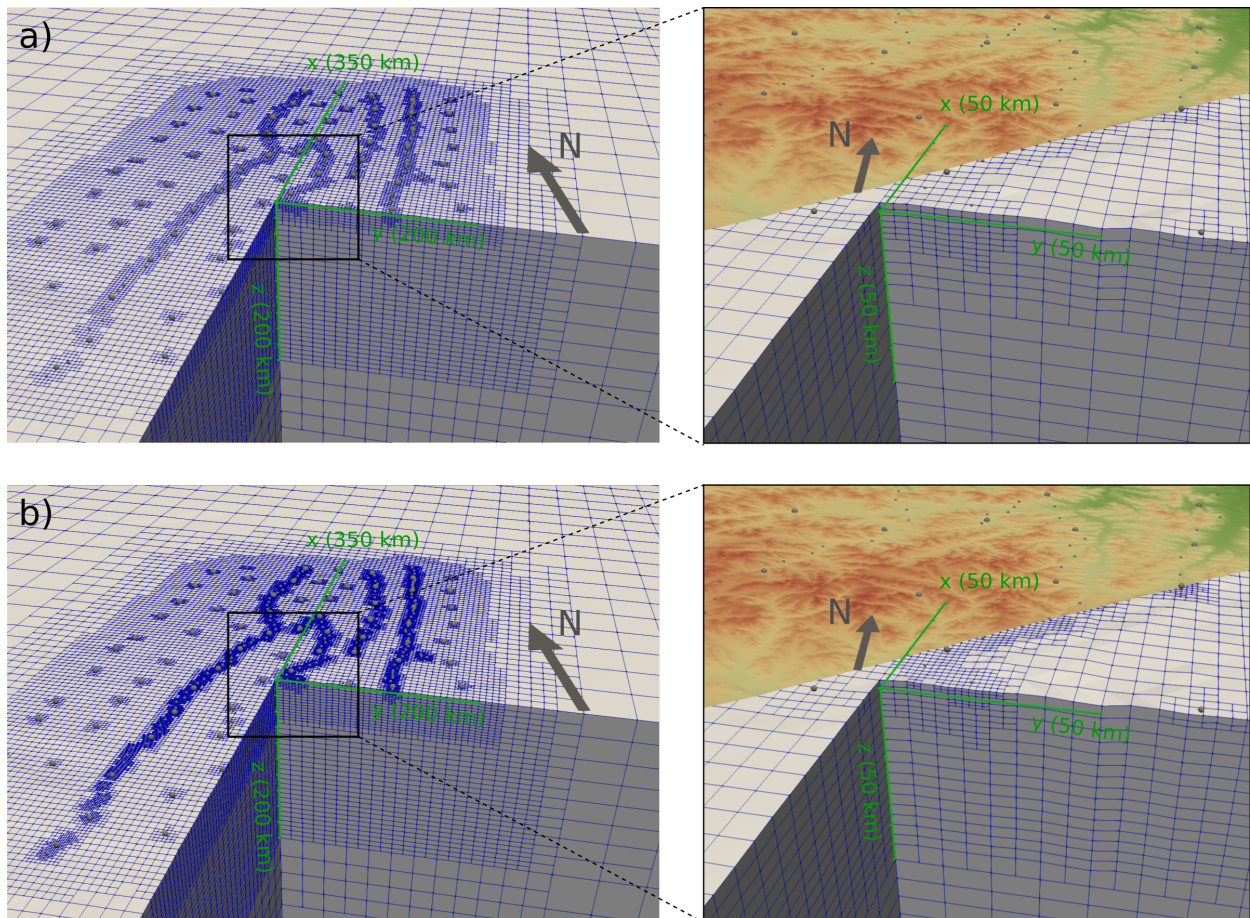


**Figure 6.** Cutaway view of the coarse (a) and fine (b) inversion meshes as well as a zoomed-in view of the central part. Local Cartesian axes (shown in green) are rotated by  $15^\circ$  clockwise from magnetic North.

### 328 3.4 Inversion methodology

329 We designed a multi-stage approach for inverting the data as shown by the flow-chart in Fig.  
 330 7. We start by inverting the regionally averaged 1-D impedance  $\bar{Z}_{1-D}$ , followed by the 3-D  
 331 inversion with increasing number of sites and a wider period band. As illustrated in Fig. 7,  
 332 the final result of each stage is used as the starting model for the subsequent stage, which  
 333 is done with a finer mesh and more data.

334 The objective function (eq. 11) has multiple minima. To prevent the inversion from  
 335 getting trapped in a local minimum that may not correspond to a geologically plausible  
 336 model, the choice of the starting model is crucial. Rung-Arunwan et al. (2016) proposed  
 337 to use a 1-D model derived from the regional 1-D impedance (eq. 7) as a starting model.



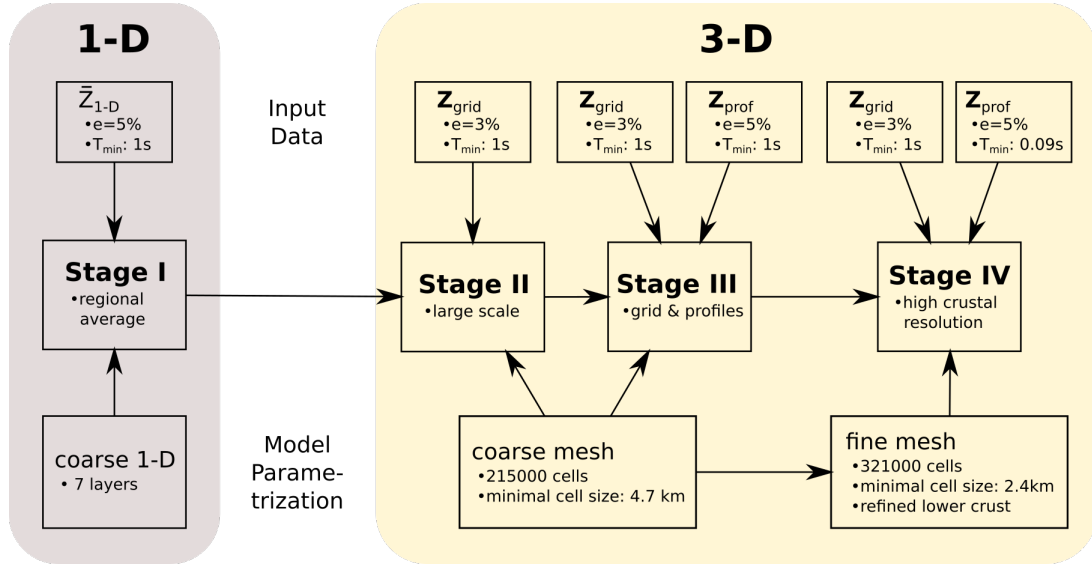


**Figure 7.** Flow chart of the inversion process, consisting of four stages with different model parametrizations and input data.  $\bar{Z}_{1-D}$  is the regionally averaged 1-D impedance (eq. 7), while  $Z_{grid}$  and  $Z_{prof}$  indicate the  $2 \times 2$  impedance tensors from grid and profile sites (see Fig. 1).  $e$  corresponds to the assigned data error (eq. 13) and the shortest period is denoted by  $T_{min}$ .

338 To calculate the regional average, we used a stochastic inversion algorithm based on the  
 339 Covariance Matrix Adaption Evolution Strategy (CMAES, see Grayver & Kuvshinov 2016),  
 340 followed by a Markov chain Monte Carlo (MCMC) walk to evaluate its uncertainty. The  
 341 obtained 1-D conductivity model is then used as an initial model for the 3-D inversion in  
 342 Stage II.

343 For Stage II, only the  $2 \times 2$  impedance tensors (with  $T > 1$  s) from quasi uniformly  
 344 spaced grid sites  $Z_{grid}$  (red sites in Fig. 1) are inverted. The resulting model is then passed  
 345 on to Stage III, where  $2 \times 2$  impedance data from the profile sites  $Z_{prof}$  (blue sites in Fig.  
 346 1) are added, most of which are telluric sites with inter-site impedance tensors estimated  
 347 using the H-field from a nearby full MT station. Based on the result from this step, the  
 348 final inversion step is performed with the finer mesh (further refinement in the lower crust)  
 349 and impedances at shorter periods ( $T > 0.09$  s). We found that this approach not only  
 350 reduces computational costs compared to running the inversion on the fine mesh directly,  
 351 but it also improves convergence significantly and enables the imaging of large and small  
 352 scale structures within a single model.

353 **4 RESULTS**354 **4.1 Stage I: regional 1-D models**

355 As outlined in Section 3.4, the regional 1-D impedances for sites north and south of the  
 356 SHF (see Fig. 3) were inverted to obtain 1-D conductivity models (see Fig. 8). The model  
 357 consists of seven homogeneous layers, consistent with the depth discretization of the 3-D  
 358 mesh. The best fit models agree with the data well. As outlined in Section 2.3,  $\bar{Z}_{1-D}$  derived  
 359 from the southern sites is likely not representative of a regional conductivity structure. As a  
 360 result, we used the 1-D model derived from the northern sites to be the starting model for  
 361 the subsequent 3-D inversion of the whole region.

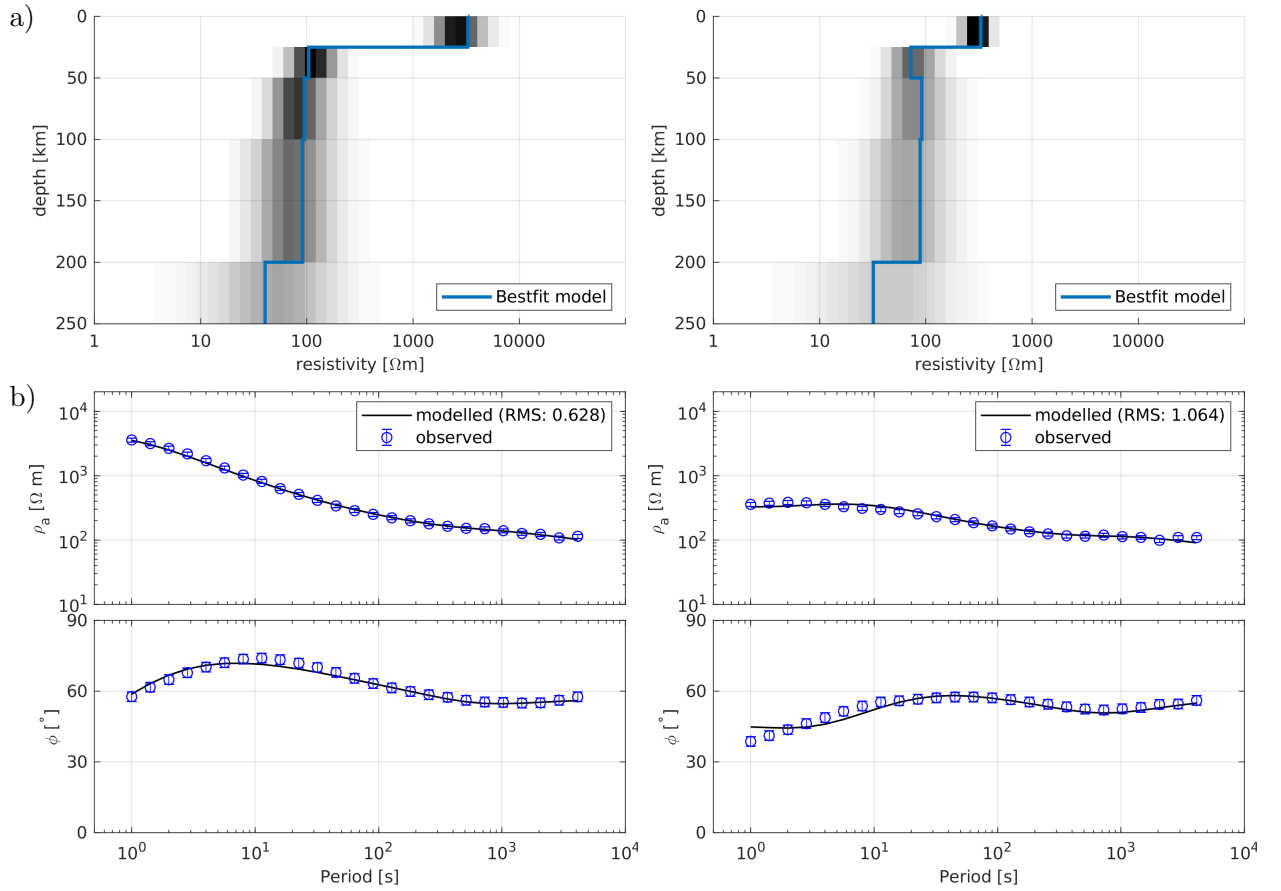


**Figure 8.** a) Regional 1-D conductivity models (blue), together with a distribution of equivalent models (grey shaded areas) for sites north (left panels) and south (right panels) of the SHF. b) Their data fit for sites north (left panels) and south (right panels) of the SHF.

## 4.2 Stage II: 3-D large-scale inversion

For this stage, only data from the grid sites (50 km nominal spacing) were inverted. Fig. 9 shows the progressive reduction of the data misfit (as defined by a root-mean squared misfit, RMS) and regularization parameter for each iteration step. As discussed in Section 3.2, the regularization parameter was decreased over the course of the inversion to permit more structure in the model. Starting from an RMS value of 43.1 using the initial 1-D model (see Section 4.1 and Fig. 8), the inversion achieved an RMS value of 2.65 after 19 iterations. Fig. 9a) shows an increase in the misfit for four out of the 19 iterations, indicating an escape from a local minimum or an overshoot, yet this did not prevent the inversion from converging. A continuation with even lower regularization resulted in negligible misfit reductions ( $< 3\%$  per iteration) and therefore the inversion was terminated.

The best-fit model (model S2) is shown in Figs 10 and 11 (see Table 1 for abbreviations of geographic and model features). The upper crust is characterised by the resistive Hangai cratonic block (HB) north of the SHF and the very heterogeneous and generally conductive Valley of Lakes (VL) south of the SHF. The Bogd fault (BF) can be traced as a strong conductor. In contrast, the Bulnay and Gobi-Altai Faults (BUF and GAF respectively) are not clearly imaged. At depths of 30 to 35 km below the Hangai, there is an abrupt drop in resistivity of three to four orders of magnitude, most likely indicating a transition to the ductile lower crust. The lower part of the crust (35 – 50 km) is a heterogeneous conductor, labelled as North, East, South, and West Hangai Conductor (NHC, EHC, SHC, and WHC, respectively). The Valley of Lakes on the other hand is underlain by a resistor (VLR). In the upper mantle (below 50 km) and above the Asthenosphere (AS), resistivities are again higher, except for the SHC and EHC. They extend vertically from the lower crust to the AS.

The single RMS value of the best fitting model is not sufficient to judge its quality (Tietze & Ritter 2013; Miensopust 2017). Instead, the results were evaluated based on the convergence (see Fig. 9), data fit distribution over periods and site locations, as well as histograms of the residuals. Fig. 12 gives a detailed breakdown of the data fit. RMS values

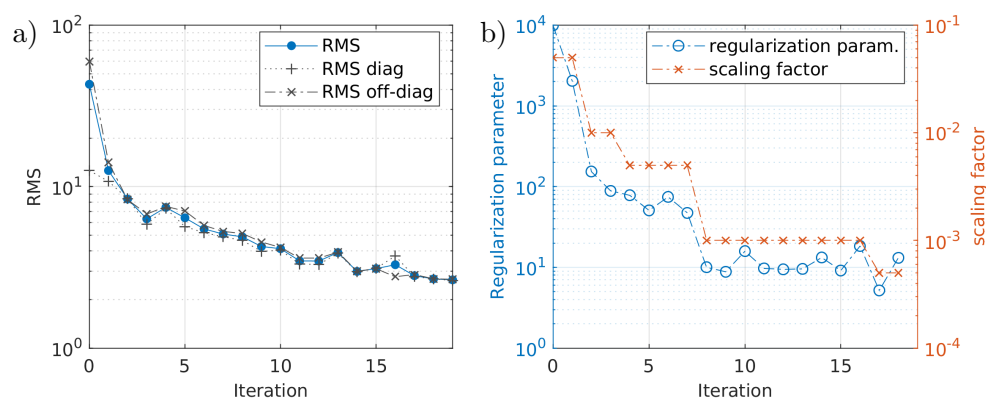


**Figure 9.** Progression of the RMS value (a) and regularization (see eq. 15) parameters (b) during Stage II of the inversion.

390 are lowest over the period range from 10 s to 1000 s with slightly higher values for shorter and  
 391 longer periods, likely because the coarse grid we use still does not allow the introduction of  
 392 structures to fit the shortest periods, whereas long period data are typically more noisy (due  
 393 to limited recording times) and difficult to fit. The misfit distribution over individual sites  
 394 is relatively uniform in the central and northern parts but generally higher in the southern  
 395 part. The southern part of the model is characterized by strong lateral resistivity variations  
 396 in the VL and the conductive BF (see the surface panel in Fig. 10). Here, coarse model  
 397 discretization and regularization prevented the introduction of stronger resistivity variations  
 398 resulting in poorer fit, which we will improve at later stages. Static shift was largely corrected  
 399 by the introduction of bow-tie shaped conductivity artefacts (see the surface panel in Fig.  
 400 10) close to the sites. Data residuals (see Fig. 12b) exhibit a symmetric and zero-centered  
 401 distribution, indicating no data-fit pathologies at this stage. The relatively large variance of  
 402 the distribution will be reduced at later stages.

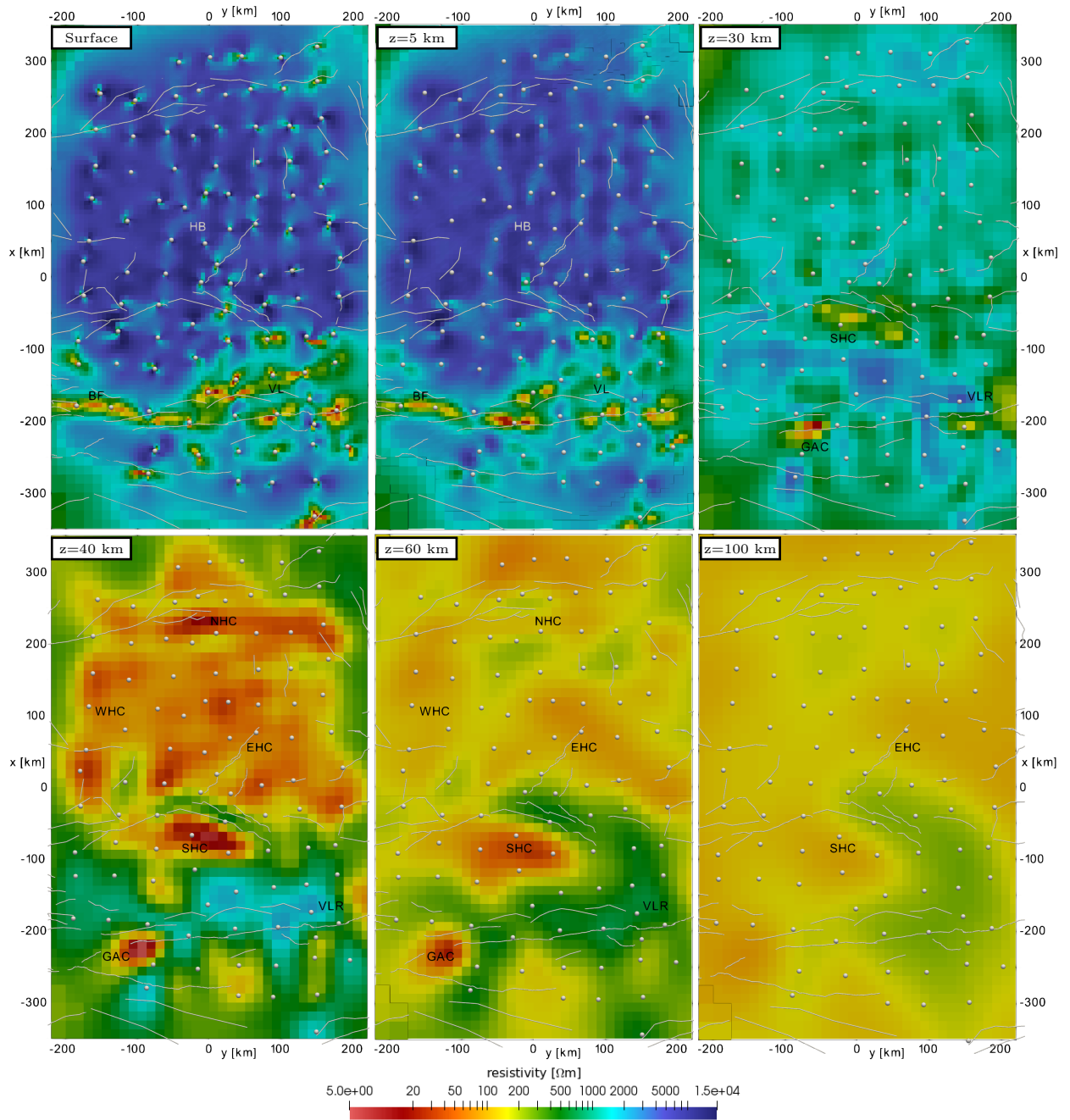


**Figure 10.** Horizontal slices through the best-fit model of inversion Stage II (model S2). Depth slices are shown at the surface and depths of  $z = 5$  km,  $z = 30$  km,  $z = 40$  km,  $z = 60$  km and  $z = 100$  km (referred to sea level). Measurement sites are marked with grey spheres and major faults with grey lines. See Table 1 for abbreviations of model features, they include the resistive HB and the heterogeneously conductive VL with the BF in the upper crust. At a depth of 30 to 40 km the resistivity drops abruptly to form five distinct conductors in the lower crust and below, the SHC, NHC, WHC, EHC and GAC. Conversely, the VL is underlain by a resistor (VLR). With greater depths resistivity rises and at 100 km only the SHC and EHC remain discernible.

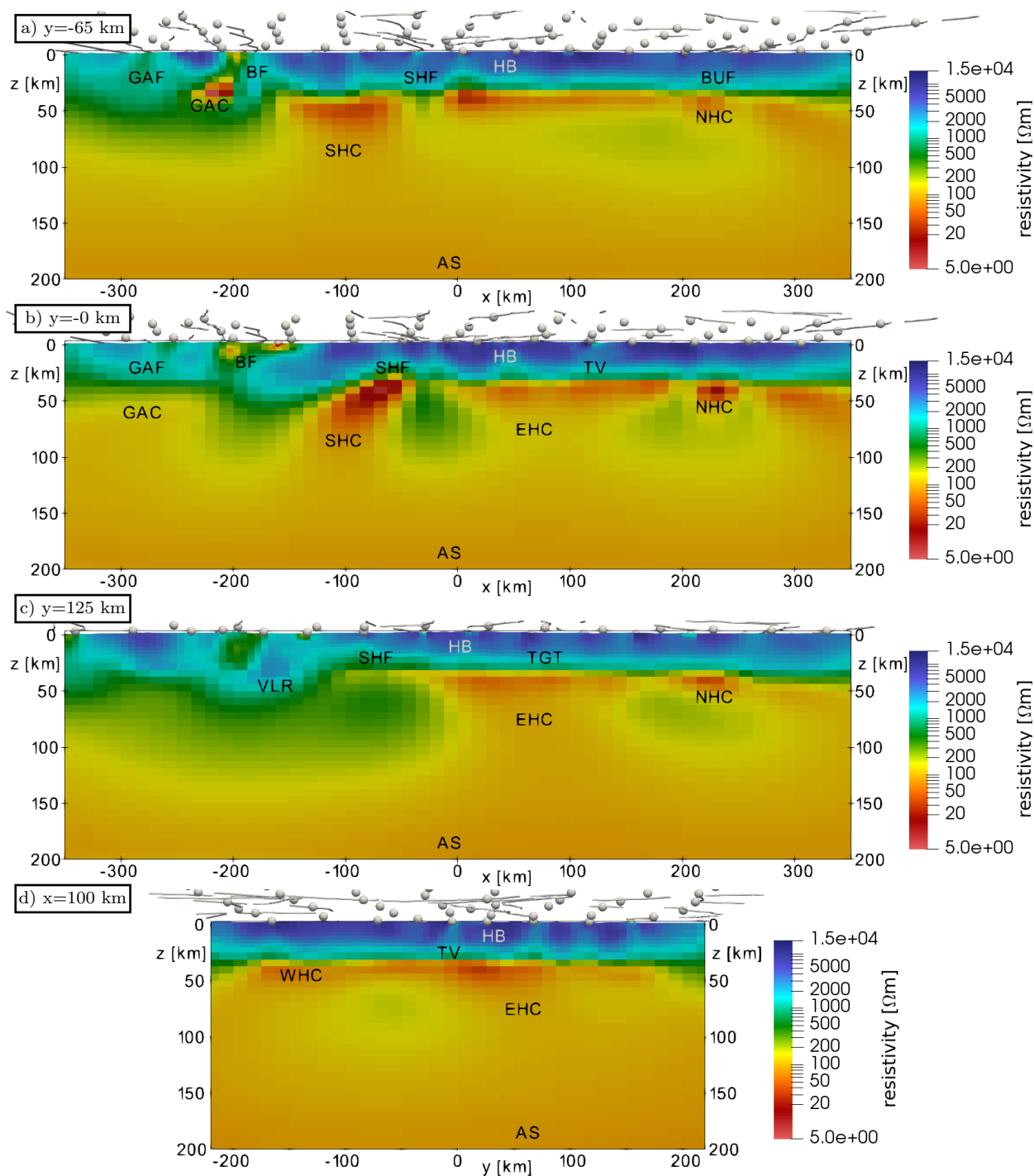


**Figure 11.** Vertical slices through the best-fit model of inversion Stage II (model S2). The slices are parallel to the x-axis at a)  $y = -65$  km, b)  $y = 0$  km, c)  $y = 125$  km (approximately aligned with profiles 2, 4, and 6, see Fig. 1), and d) parallel to the y-axis at  $x = 100$  km. Measurement sites are marked with grey spheres and major faults with grey lines. See Table 1 for abbreviations. The conductive BF can clearly be seen in the upper crust, whereas the GAF and SHF only show up as faint near-surface conductors. Additionally, it can be seen that the NHC is confined to a depth of 40 to 60 km (the lower-most crust), while the EHC and SHC extend downward to the AS. See also Fig. 10 for major model features.

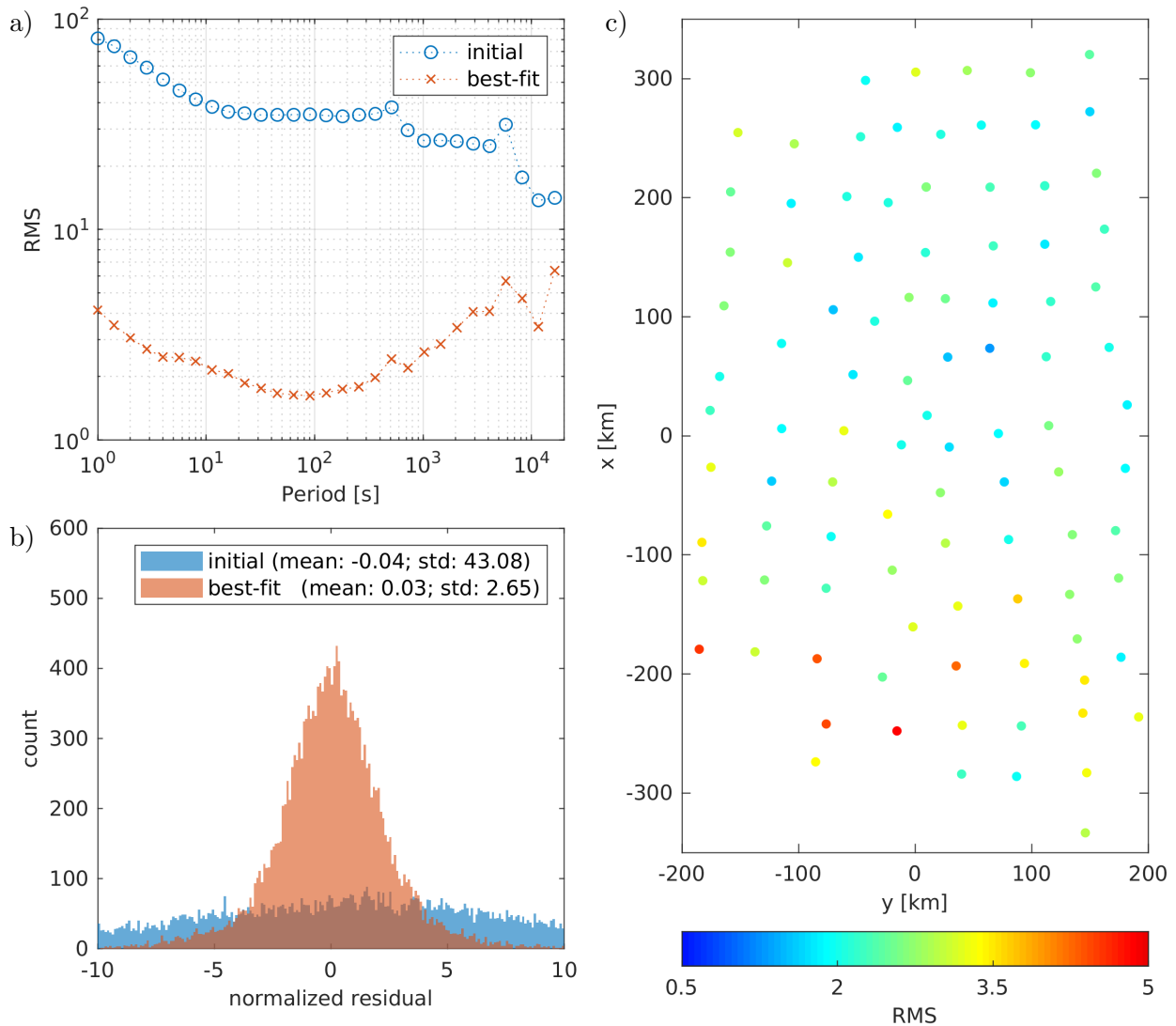


**Figure 12.** Data fit distribution of inversion Stage II. a) RMS value across periods for the initial and best-fit model; b) data residual histogram for the initial and best-fit model; c) RMS values at measurement sites for the best-fit model.

### 4.3 Stage III: 3-D inversion of all measurement sites

For the third stage, all measurement sites along profiles and near the TV and TGT were included (mostly telluric-only data). Adding the new data to the previous best fit 3-D model increased the RMS value to 33. After 12 iterations the inversion converged to a model with a RMS value of 2.1. Fig. 13 shows that an RMS value of 3 was reached after only four iterations, owing mostly to the compensated static shift effect. The best fit model (model S3) is shown in Figs. 14 and 15. In comparison to the results from the previous stage (Figs 10

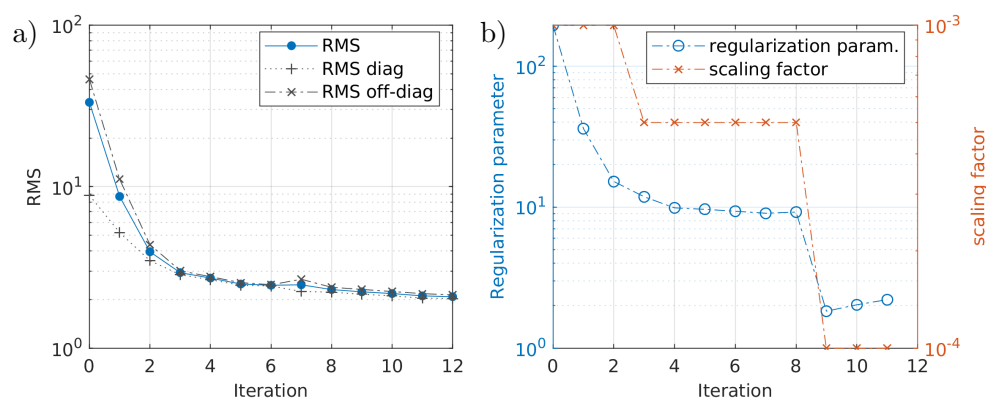


**Figure 13.** Progression of the RMS value (a) and regularization (see eq. 15) parameters (b) during Stage III of the inversion.

410 and 11), the large-scale structure remains the same, but resistivity contrasts became better  
 411 resolved and some crustal structures appear more pronounced, such as the peculiar shape of  
 412 the NHC. Additionally, the upper crustal resolution is improved (GAF, BF, and SHF) and  
 413 new structures appear, for example the lowered resistivity in the upper crust below the TV  
 414 and the TGT.

415 With a RMS value of 2.1, the data fit (Fig. 16) is overall better than in the previous  
 416 stage, but with the same characteristics. Specifically, the misfit is slightly higher for short  
 417 and long periods as well as for the southern sites. Additionally, there are three sites on profile  
 418 P2 and two sites on profile P4 with a significantly higher misfit. These remaining problems  
 419 are mainly due to the complex local 3-D structures and are resolved in the final stage of the  
 420 inversion.



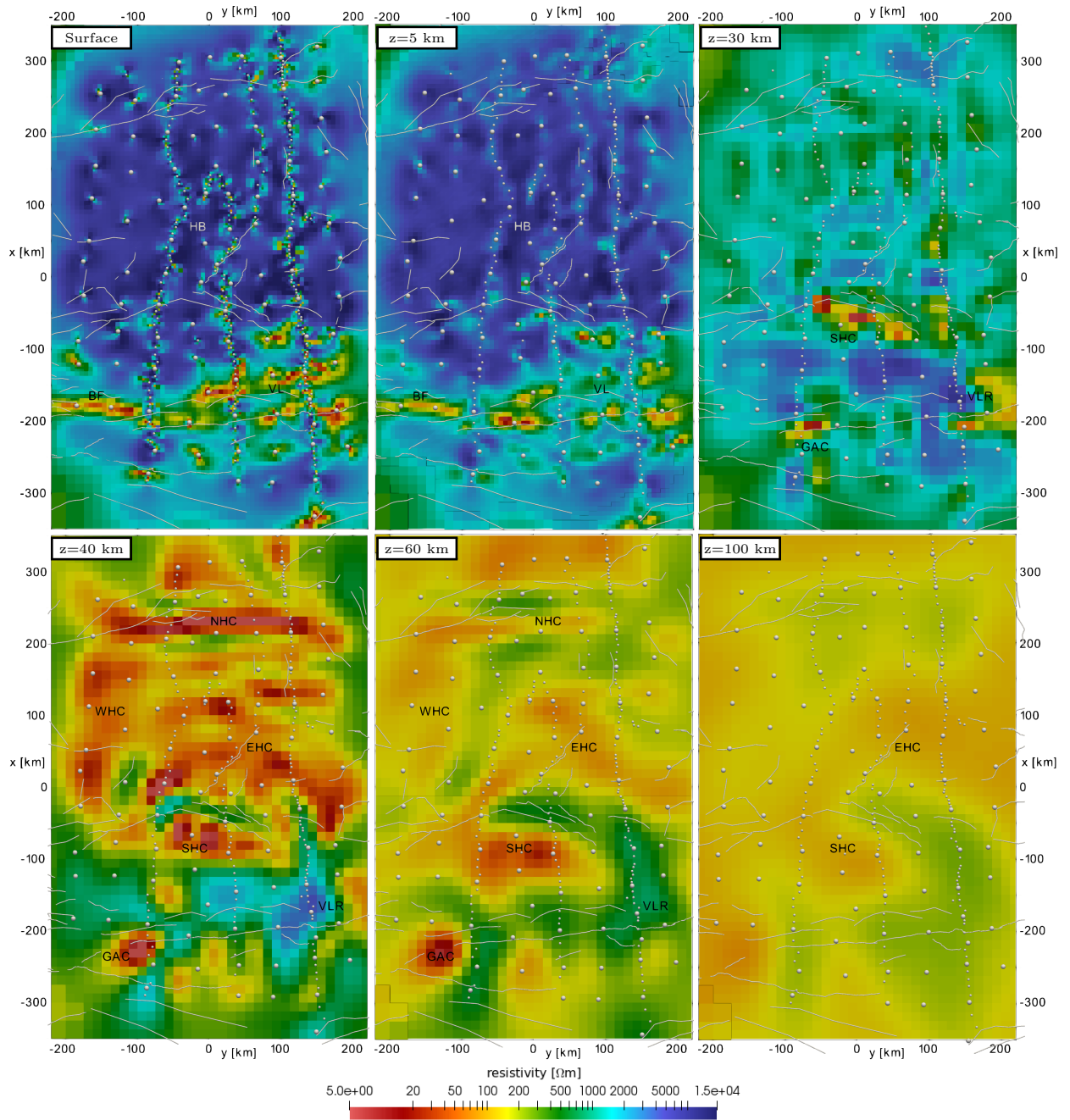


**Figure 14.** Horizontal slices through the best-fit model of inversion Stage III (model S3). Depth slices are shown at the surface and depths of  $z = 5$  km,  $z = 30$  km,  $z = 40$  km,  $z = 60$  km and  $z = 100$  km (referred to sea level). Measurement sites are marked with grey spheres and major faults with grey lines. See Table 1 for abbreviations of model features. In comparison to the previous stage (see Fig. 10), model features are imaged more finely. The near surface along the profiles and the conductors in the lower crust ( $z = 40$  km) especially benefit from the additional data included in this stage.

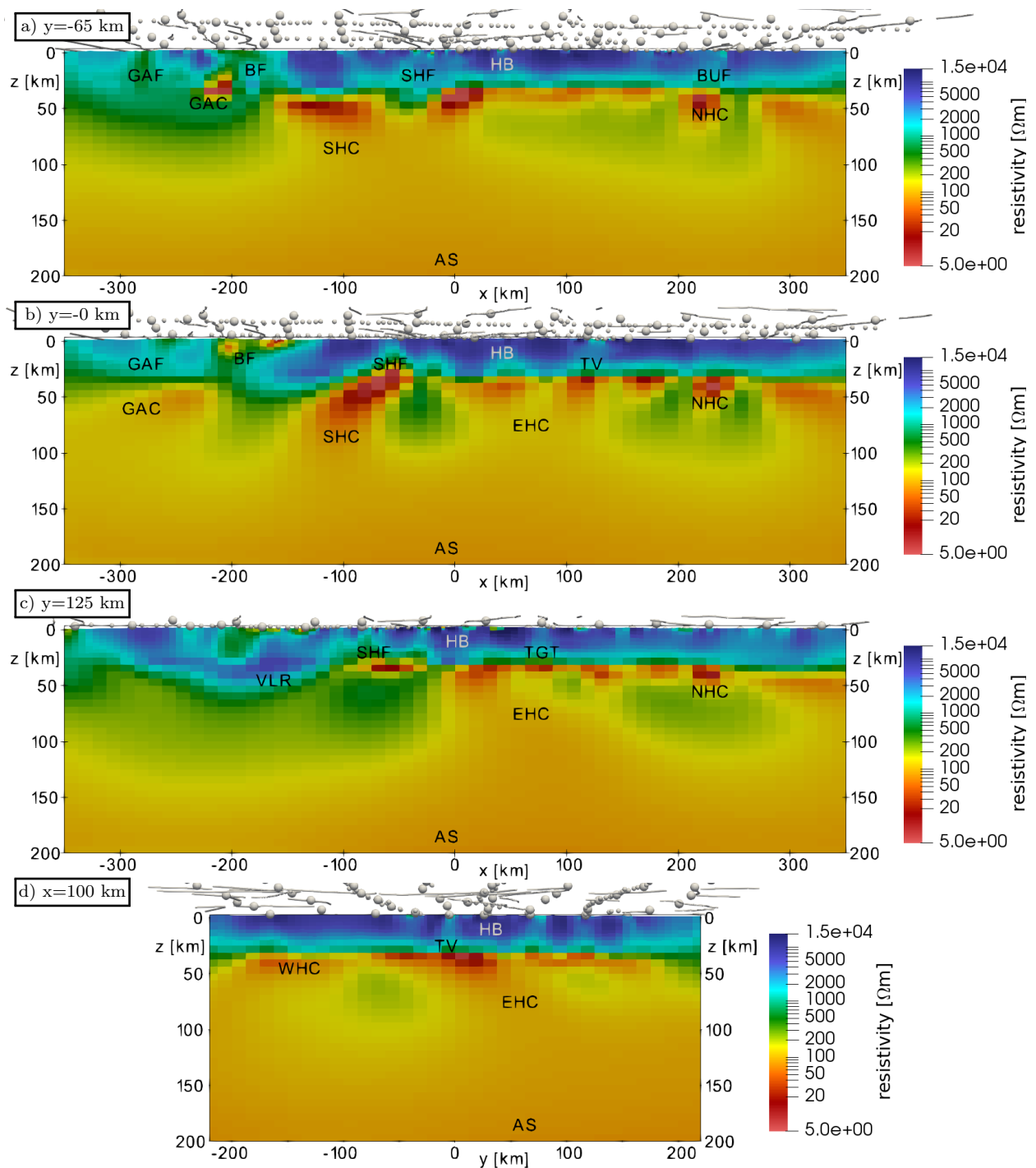


**Figure 15.** Vertical slices through the best-fit model of inversion Stage III (model S3). The slices are parallel to the  $x$ -axis at a)  $y = -65$  km, b)  $y = 0$  km, c)  $y = 125$  km (approximately aligned with profiles 2, 4, and 6, see Fig. 1), and d) parallel to the  $y$ -axis at  $x = 100$  km. Measurement sites are marked with grey spheres and major faults with grey lines. See Table 1 for abbreviations of model features. See Fig. 10 for major model features. In this model, conductive signatures can be seen in the upper crust below TV and TGT.

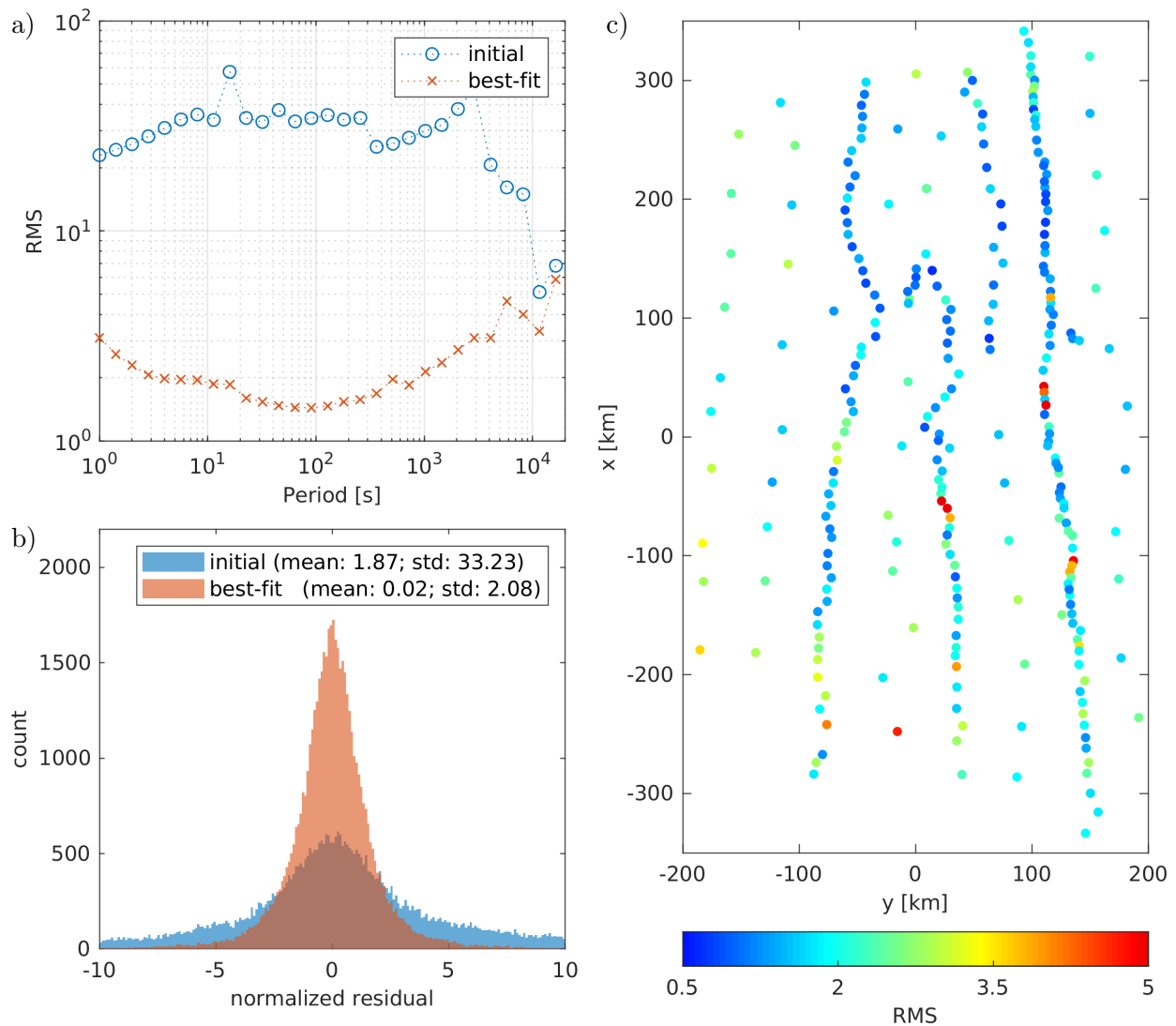


**Figure 16.** Data fit distribution of inversion Stage III. a) RMS value across periods for the initial and best-fit model; b) data residual histogram for the initial and best-fit model; c) RMS values at measurement sites for the best-fit model.

#### 4.4 Stage IV: higher crustal resolution and short periods

For the last stage, short period data along the denser profiles were added and a finer mesh was used. As we will see, the mesh refinement around site locations and in the lower crust leads to a better fit for short period data.

Adding new data increases the RMS to a value of 8.9 when using the best fitting model from the previous stage. After 17 iterations a misfit of 1.86 was obtained (see Fig. 17). The resulting model (model S4) is shown in Figs 18 and 19. Compared to the previous stage,

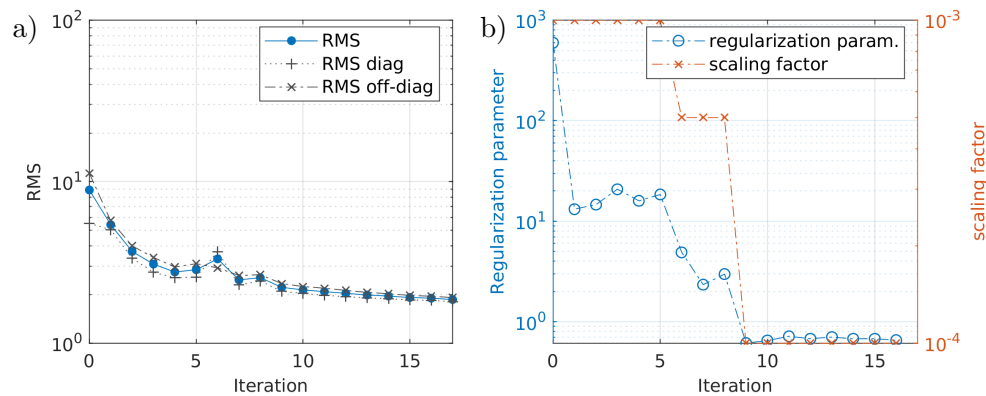


**Figure 17.** Progression of the RMS value (a) and regularization (see eq. 15) parameters (b) during Stage IV of the inversion.

428 the finer mesh leads to significantly improved resolution in the lower crust, which further  
 429 enhanced the geometry and structure of the lower crustal conductors (NHC, EHC, SHC and  
 430 WHC). By adding the short period data, the crust is imaged more finely and the resolution  
 431 is close to that of the 2-D model by Comeau et al. (2018c).

432 The model fits the data well (Fig. 20). The overall higher misfit at longer periods (>  
 433 1000 s, Fig. 20a) can be attributed to noisy long period data and the fact that the assigned  
 434 error was likely too optimistic for these periods. Additionally, there are eight sites that  
 435 have a RMS values > 3.5, either due to noisy data and poor fit of the diagonal impedance  
 436 components or because of unresolved local structures.

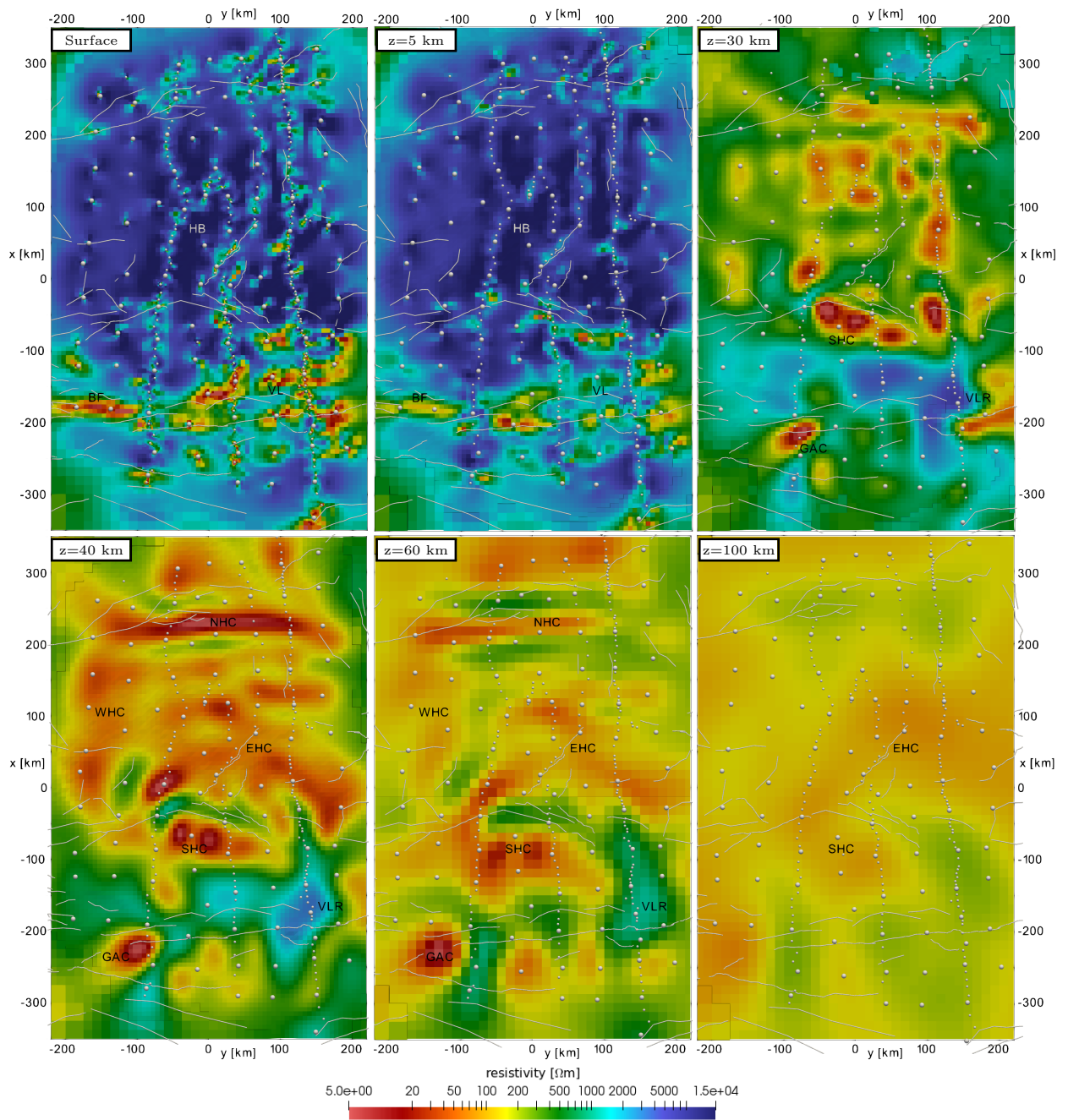


**Figure 18.** Horizontal slices through the final model of inversion Stage IV (model S4). Depth slices are shown at the surface and depths of  $z = 5$  km,  $z = 30$  km,  $z = 40$  km,  $z = 60$  km and  $z = 100$  km (referred to sea level). Measurement sites are marked with grey spheres and major faults with grey lines. See Table 1 for abbreviations and Figs 10 and 14 for the model features.

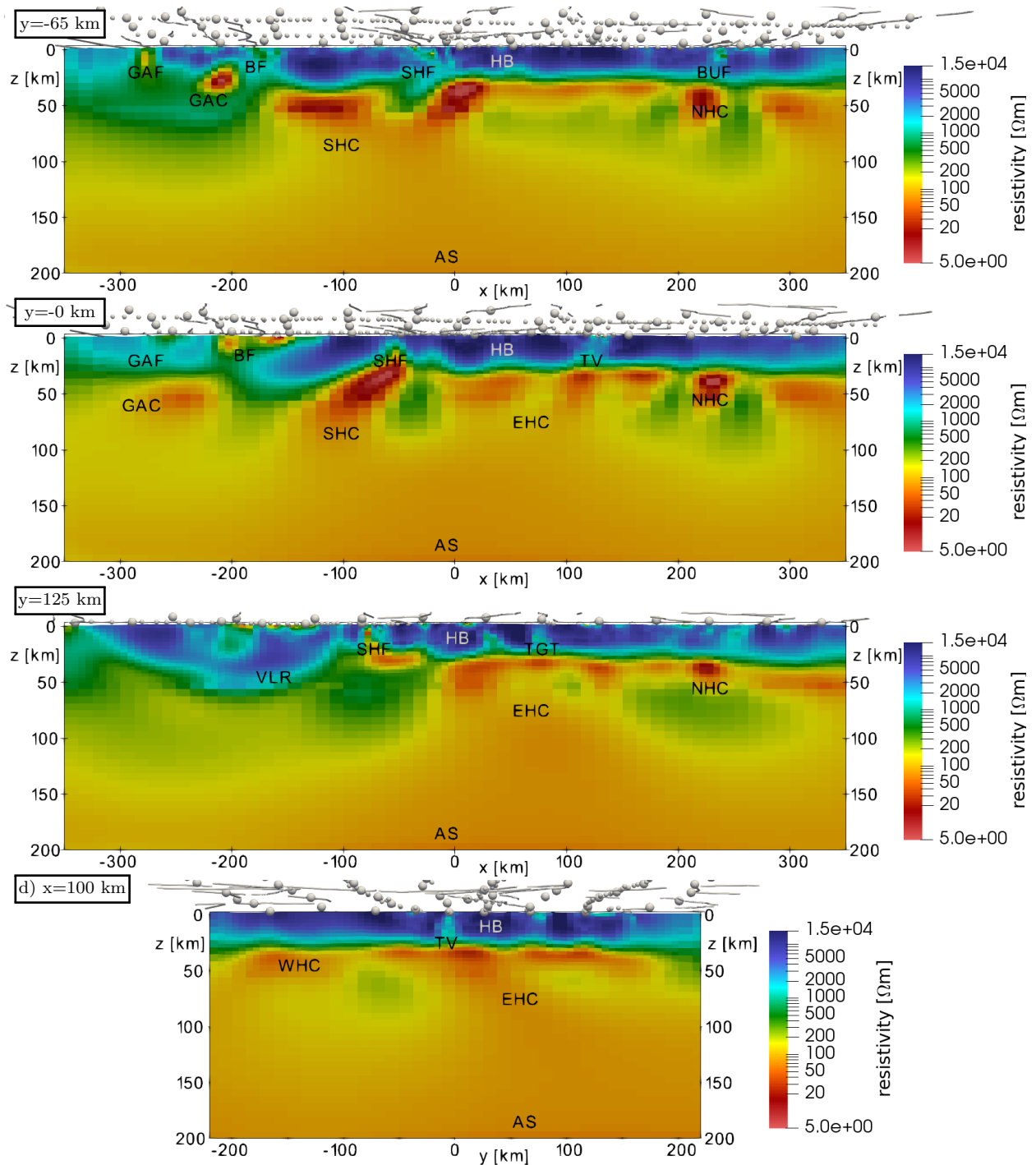


**Figure 19.** Vertical slices through the final model inversion Stage IV (model S4). The slices are parallel to the x-axis at a)  $y = -65$  km, b)  $y = 0$  km, c)  $y = 125$  km (approximately aligned with profiles 2, 4, and 6, see Fig. 1), and d) parallel to the y-axis at  $x = 100$  km. Measurement sites are marked with grey spheres and major faults with grey lines. See Table 1 for abbreviations and Figs 11 and 15 for model features. During this stage the BUF was resolved in some parts of the model.



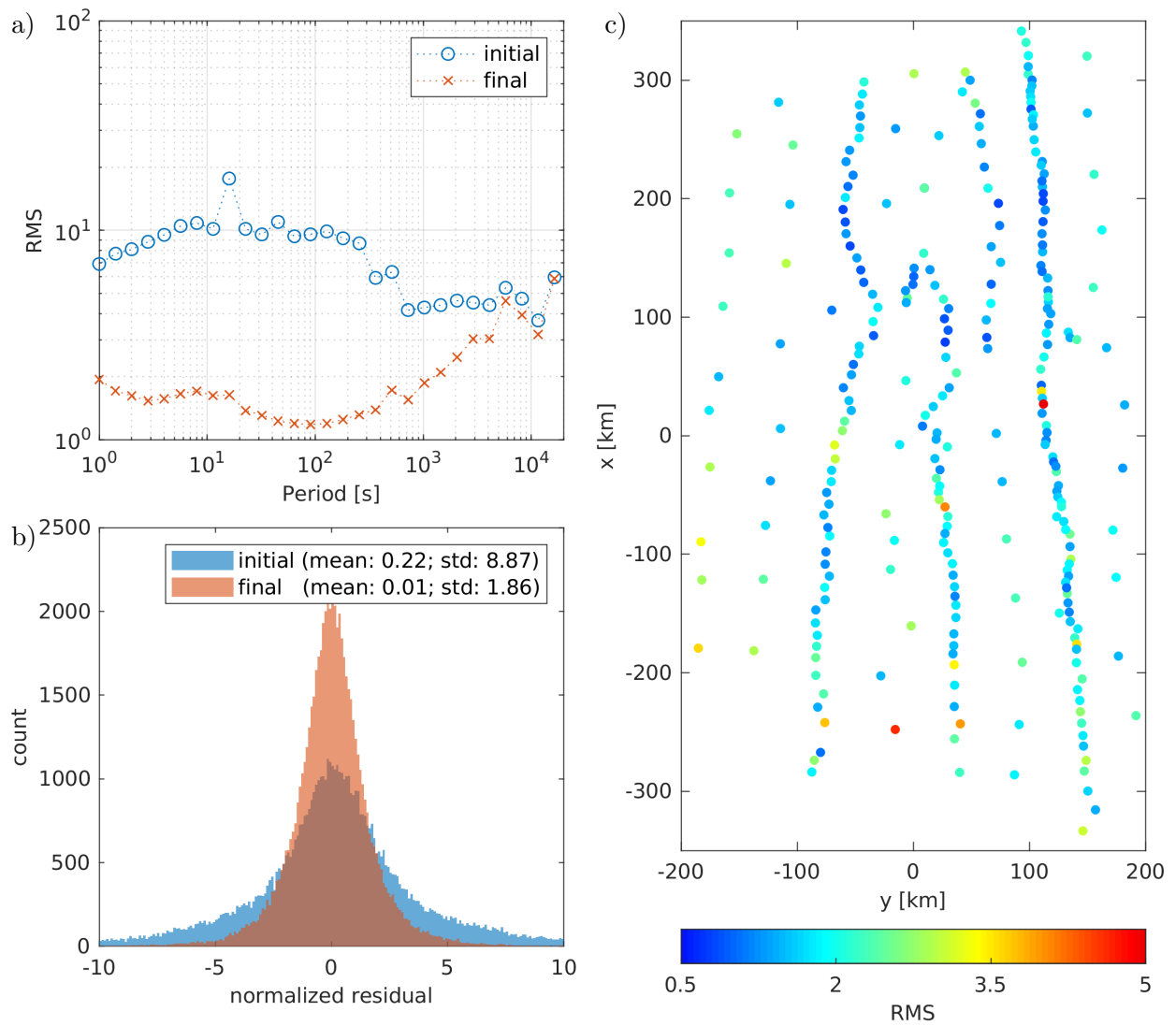


**Figure 20.** Data fit distribution of inversion Stage IV. a) RMS value across periods for the initial and final model; b) data residual histogram for the initial and final model; c) RMS values at measurement sites for the final model.

## 5 DISCUSSION

### 5.1 Inversion methodology

In the previous section, we explained the four stage inversion strategy used to obtain the final resistivity model. Fig. 21 shows a comparison of the models S2, S3, and S4 for an example area in the centre of the model. While larger features (HB, EHC, SHC, etc.) are already imaged in Stage II, the addition of profile sites during Stage III reveals smaller crustal features in more detail (SHF, TV, etc.) and gives a finer resolution for the structure of the EHC in model S3. Additional mesh refinement and the inclusion of short period data improves the results further, as is evident by the comparison of S3 and S4. The link between the SHC and SHF can be seen and TV becomes a prominent vertical conductor in the upper crust, located directly on top of a 40  $\Omega\text{m}$  conductor at a depth of 35 km. Similar improvements from stage to stage can be observed for other features throughout the model (e.g. TGT, GAF, BUF, BF, CV).

During the first stage, a regionally averaged 1-D model was derived to be used as an initial model for the 3-D inversion. It is well known that the initial model can significantly influence the result of a 3-D inversion. To assess the influence of the 1-D model, we performed two inversion runs with identical settings to Stage II except for initial half-space models of 500  $\Omega\text{m}$  (Model S2HS500) and 1000  $\Omega\text{m}$  (Model S2HS1000), see the supplementary material Sec. S3.1 and S3.2. After 18 iterations S2HS500 achieved a RMS value of 3.1 and S2HS1000 achieved a RMS value of 3.2 after 19 iterations. Both are significantly higher than the RMS value of 2.65 achieved after Stage II with a 1-D starting model (Sec. 4.2).

The recovered conductivity structure is similar to S2 only down to a depth of about 70 to 100 km. Below that depth no new features were introduced. Furthermore, it can be seen that the arbitrary choice of the initial half-space resistivity influences the overall resistivity of the final model, the average resistivity of S2HS500 is lower than that of S2HS1000. Although the initial 1-D model from Stage I has an influence on the results of Stage II, there is no arbitrary choice of resistivity values. Instead, the initial model is defined by the regionally averaged



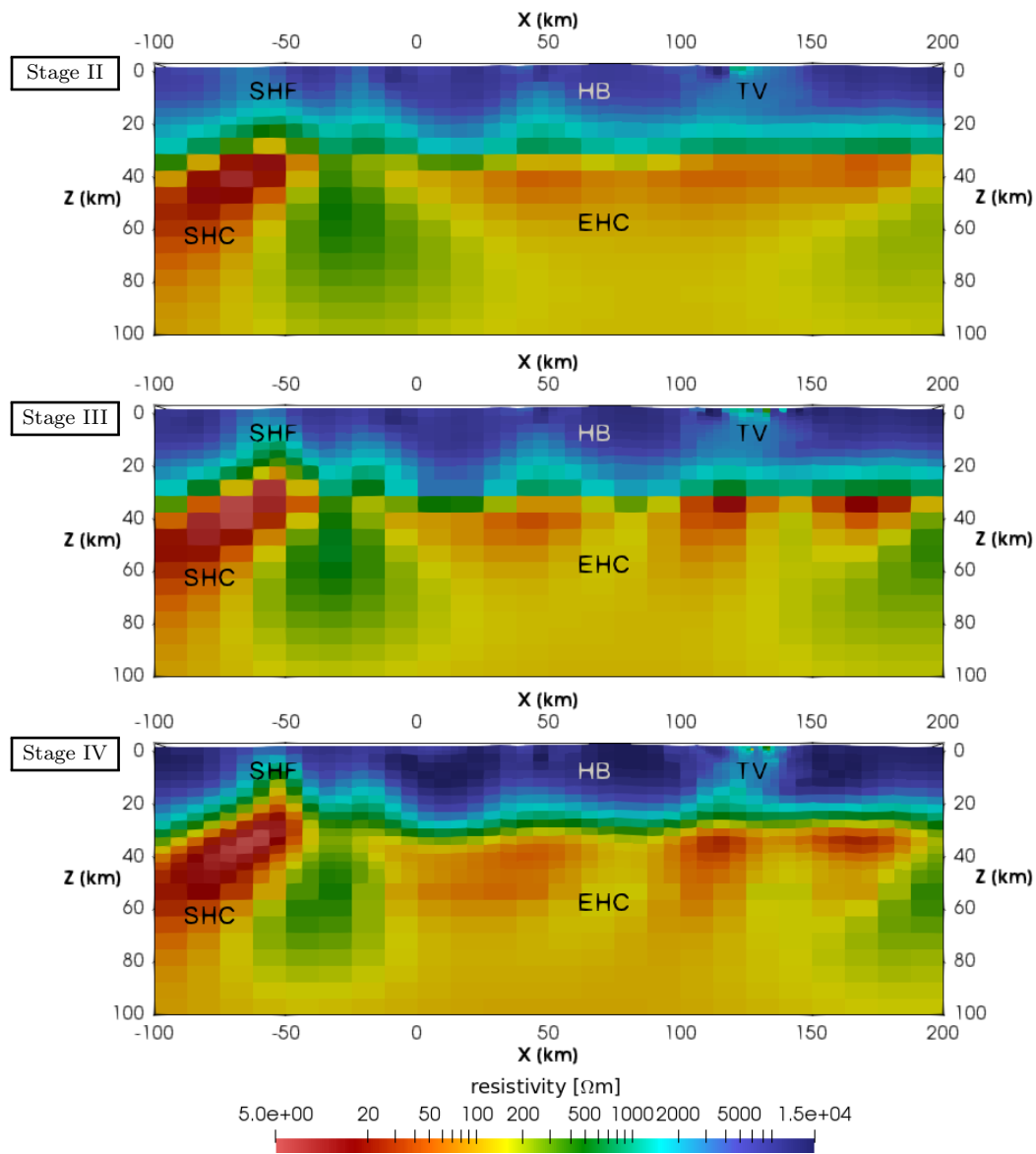


**Figure 21.** Comparison of the three stages of the 3-D inversion on a vertical slice in x-direction at  $y = 0$ . See Table 1 for abbreviations and Figs 11, 15, and 19 for major model features.

464 impedances and represents the best-fitting 1-D model, with the caveat that measurement  
 465 sites south of the SHF were discarded (due to the lack of a consistent regional 1-D structure,  
 466 as outlined in the Sections 4.1 and 2.3). The regional 1-D model north of the SHF is thereby  
 467 imposed on the region in the south. However, this proves to be not a problem because the  
 468 1-D model enters Stage II only as an initial model, not as a reference for the regularization.  
 469 The strong conductivity contrast at  $z = 25$  km (see Fig. 8) is almost completely removed  
 470 and a laterally more heterogeneous resistivity structure is introduced for the VL and the  
 471 region south of the SHF to fit the data there.

472 Separate inversion Stages II and III were necessary to ensure that the regional resistivity  
473 structure was recovered first, before smaller and shallow structures were fitted. If the Stages  
474 II and III are combined (see Model S2+3 in the supplementary material S3.3) the inversion  
475 is strongly biased to the eastern part of the grid (between P2 and P6, see Fig. 1) due to the  
476 higher number of stations there. This leads to the western part of S2+3 (west of P6) being  
477 fitted only in the end of the inversion process (starting at iteration 15 of 23), resulting in  
478 a significantly higher RMS value for sites along line 8, in comparison with the entire grid.  
479 The recovered model happens to be virtually identical to model S3. However, because of the  
480 bias to the eastern sites for most of the iteration steps, a separated approach is preferred,  
481 whereby the regional 3-D structure is recovered from the grid stations first, and afterwards  
482 smaller structures are revealed due to the additional data from the profiles introduced during  
483 Stage III.

484 For the same reason, short period data (0.09 s to 1 s) with penetration depths as small  
485 as 2 km were added in Stage IV, the final stage of the inversion process. The short period  
486 data were accompanied by a mesh refinement, which increased the computational cost of  
487 a single iteration by a factor of 2.4. By fitting the regional structure on the coarser mesh  
488 first and using the fine mesh only in the end, the computational cost for the entire inversion  
489 process was significantly reduced.

## 490 **5.2 Description of observed features**

### 491 *5.2.1 Upper mantle features*

492 The final 3-D resistivity model images a pervasive low-resistivity feature (30–100  $\Omega\text{m}$ ) at  
493 depths greater than 150 km (AS; see Figs 19 and 22). To the south, below the South Gobi  
494 region, this feature appears at depths of approximately 130 km. Whereas below the Hangai  
495 Dome, this feature appears to shallow to depths of approximately 70 km (SHC and EHC;  
496 see Figs 19 and 22). This is consistent with previous 2-D models (Comeau et al., 2018c;  
497 Comeau et al., 2019b). However, what is unique in the 3-D model presented here is that the  
498 non-uniformness and lateral complexity of the feature is imaged. This low-resistivity feature

500 has two regions that shallow and bulge upwards: one region below the eastern Hangai Dome  
501 (EHC; see Fig. 22) that dips eastward, and a smaller region located slightly south of the  
502 Hangai Dome (SHC; see Fig. 23).

503 Previous seismic profile measurements indicated an irregular, dome-shaped lithosphere-  
504 asthenosphere boundary (LAB) below central Mongolia that varies from 70–130 km depth  
505 (Petit et al. 2008), and a deep ( $< 150$  km) low-velocity zone below the eastern Hangai  
506 (Chen et al. 2015; Zhang et al. 2017). Bouguer gravity models revealed a localized low-  
507 density structure at a depth of 80–125 km below the central Hangai (Tiberi et al. 2008,  
508 see Fig. 1). Furthermore, analysis of erupted xenoliths from intraplate volcanism in central  
509 Mongolia suggests long-lived ( $< 30$  Ma) and shallow ( $< 70$  km) melting of an asthenospheric  
510 source (Ionov 2002; Barry et al. 2003; Hunt et al. 2012).

511 Broad array coverage and the inclusion of long-period data in the resistivity model yield  
512 sensitivity to the asthenosphere (confer Fig. 3). Based on the available evidence, the deep,  
513 low-resistivity feature may be explained by a non-uniform LAB with small, localized up-  
514 wellings. The moderate resistivity values observed in the final model can be explained by  
515 low-percent partial melts (Comeau et al. 2018c), possibly generated by decompression melt-  
516 ing from a small-scale asthenospheric upwelling. Comeau et al. (2018c) calculated more than  
517 3% melt was required to explain the resistivity values observed in the mantle, consistent with  
518 geochemical estimates of 2–7% from lava samples (Hunt et al. 2012; Ancuta et al. 2018).

519 The EHC lies below the eastern Hangai Dome, a region of elevated topography and the  
520 location of many Cenozoic volcanic provinces (Ancuta et al. 2018, see Fig. 1), elevated heat-  
521 flow measurements (Ionov 2002, and references therein, see Fig. 1), and a high concentration  
522 of present-day hydrothermal activity in the form of meteoric hot springs (Ganbat & Demberel  
523 2010; Oyuntsetseg et al. 2015, see Fig. 1). In contrast, in the western part of the Hangai  
524 Dome, despite its topographic similarity to the eastern part, there are few signs of volcanism  
525 and hydrothermal activity. The SHC lies below a topographic high slightly south of the  
526 Hangai Dome. Both the EHC and SHC are connected with a continuous low-resistivity  
527 region below 150 km. It is not known whether there exists similar regions, for example

below the Hovsgol rift and volcanic region in northern Mongolia, and if so, how they are connected at depth.

The origin of a small-scale asthenospheric upwelling remains purely speculative at this time. Historically, explanations for intra-continental uplift have been dominated by arguments for hot, mantle-rooted plumes (e.g. Windley & Allen 1993). However, modern geophysical and petrological evidence in central Mongolia is not consistent with this explanation (e.g. Barry et al. 2003). Alternative explanations include edge-driven convection resulting from a lithospheric step near the Siberian Craton that could cause thermal erosion of the lithosphere (as in Bao et al. 2014), or thinning of the lithosphere by a delamination process, whereby dense sub-crustal lithosphere decouples and peels away from the crust (Bird 1979; Kay & Kay 1993; Meissner & Mooney 1998). The latter explanation may account for other observational constraints in central Mongolia, such as the intracontinental uplift of the Hangai Dome and the long-lived mantle melting responsible for intraplate volcanism. Furthermore, numerical modelling studies indicate that a weak lower-most crust is required to trigger a delamination event (Krystopowicz & Currie 2013), consistent with observations in central Mongolia (see below; Vergnolle et al. 2003).

### *5.2.2 Lower crustal structure*

The final 3-D resistivity model images a prominent, heterogeneous low-resistivity zone (5–50  $\Omega\text{m}$ ) in the lower crust (30–50 km; NHC, WHC, EHC, and SHC in Figs 18 and 19). It is well-resolved because it is overlain by a highly-resistive feature ( $> 2000 \Omega\text{m}$ ; HB) and is a robust modelling result at all inversion stages (see Fig. 21). This feature is pervasive throughout the central Hangai but ends abruptly at the South Hangai fault zone (SHF; see Fig. 19). In the northern Hangai region this heterogeneous low-resistivity zone is roughly organized into several east-west trending tubes (e.g., NHC; see Fig. 18), roughly parallel to the Bolnay fault zone. The tube-like conductors ( $< 50 \Omega\text{m}$ ) have a nearly equal width and separation of approximately 25 km.

Crustal low-resistivity zones can be explained by local accumulations of conductive fluids

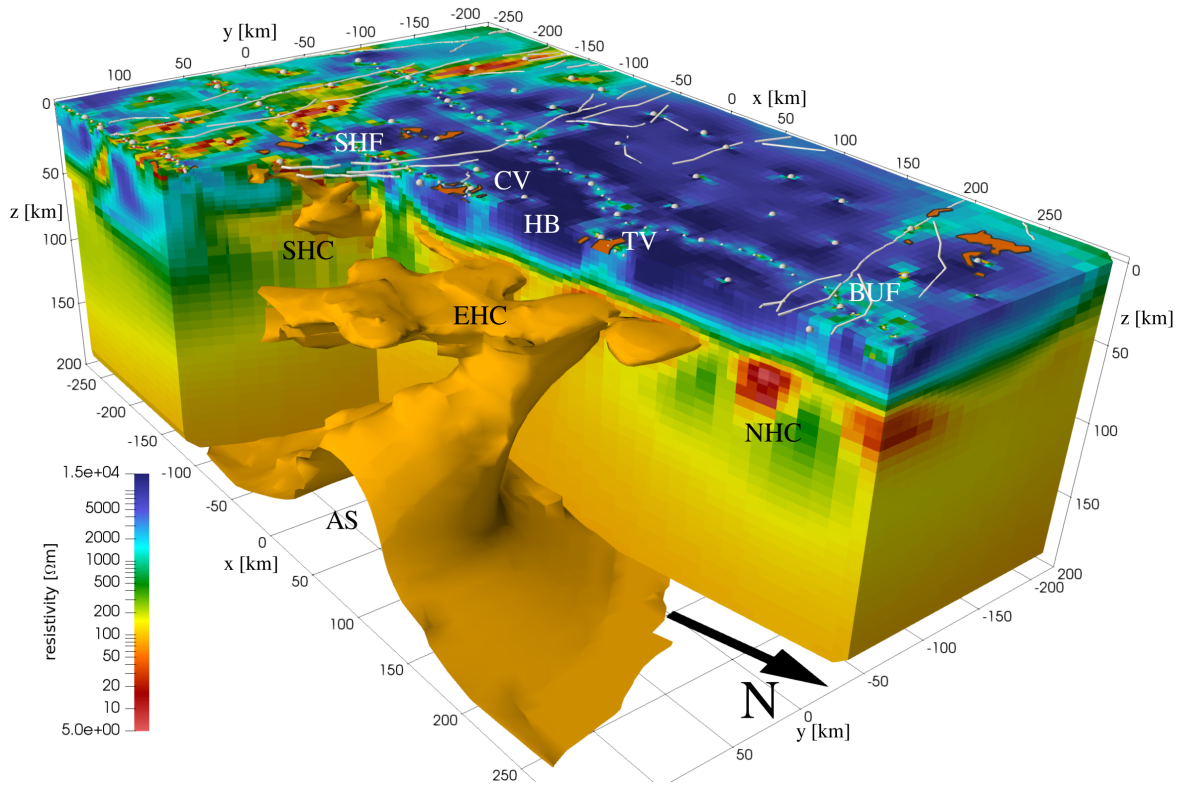


**Figure 22.** 3-D cutaway view of the model S4. The EHC and the eastern arm of the asthenospheric upwelling are shown with a  $85 \Omega\text{m}$  isosurface. White spheres indicate measurement sites, white lines are faults, and volcanic provinces are orange.

554 (e.g. Unsworth & Rondenay 2013). Geochemical evidence indicates that lithospheric meta-  
 555 somatism occurred in Mongolia due to the closure of the Mongol-Okhotsk ocean (Sheldrick  
 556 et al. 2019) and highly saline fluids can be exsolved by metasomatism in dehydration and  
 557 devolatilisation reactions (Manning 2018). Fluid content substantially changes the rheology  
 558 and significantly reduces crustal strength and viscosity (e.g. Liu & Hasterok 2016). This is  
 559 consistent with evidence from post-seismic slip measurements that indicate a significantly  
 560 reduced viscosity in the lower crust of Mongolia, of several orders of magnitude, as compared  
 561 to the upper crust (Vergnolle et al. 2003).

562 The location of these low-resistivity zones can be explained by a conceptual model that  
 563 predicts that in compressive tectonic settings (as in central Mongolia) an inverted stress  
 564 gradient beneath the brittle-ductile transition causes fluids to become trapped in the lower  
 565 crust (Connolly & Podladchikov 2004). Furthermore, numerical hydromechanical models can

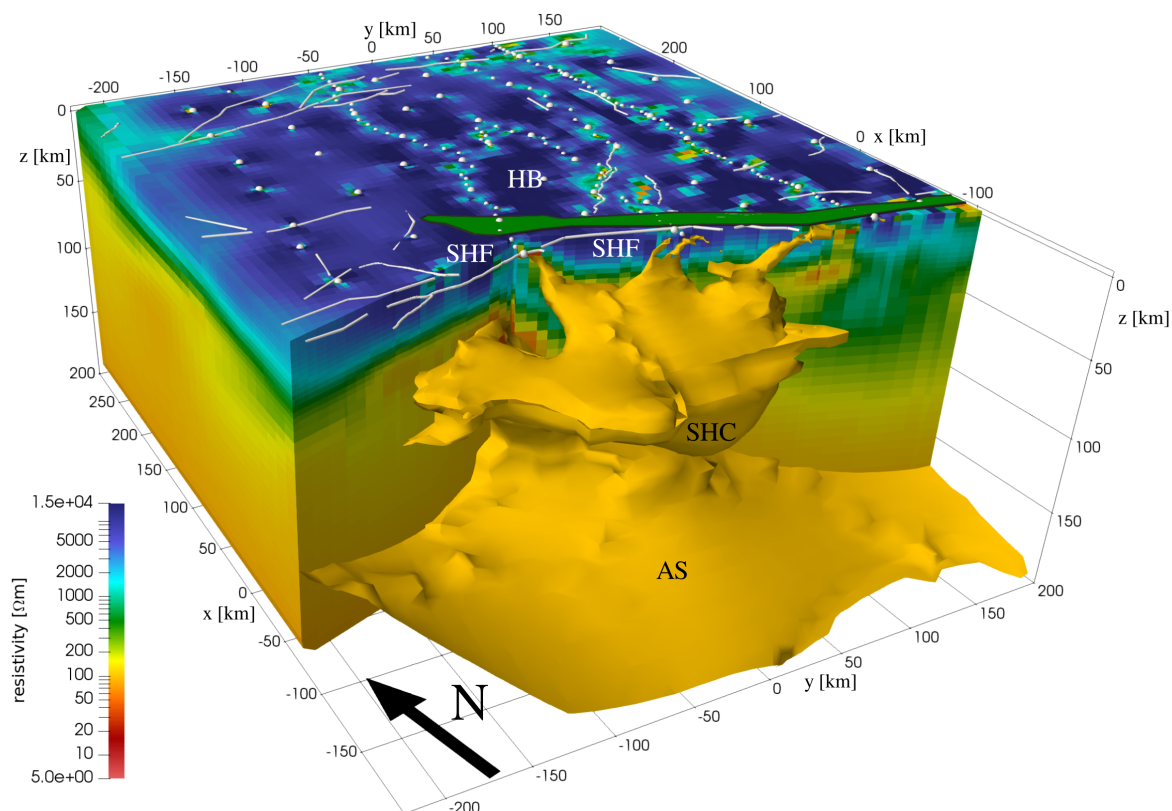


**Figure 23.** 3-D cutaway view of the model S4. The SHC and the southern arm of the asthenospheric upwelling are shown with a  $100 \Omega\text{m}$  isosurface. White spheres indicate measurement sites, white lines are faults, and the green area is the Bayankhongor Ophiolite Belt (Buchan et al. 2001).

566 explain how spatial focusing of the fluid source flux can create hydraulically connected, fluid-  
 567 rich domains within the ductile crust (Connolly & Podladchikov 2013; Comeau et al. 2019a).  
 568 In addition, the pattern of fluid focusing is expected to be superimposed on large-scale  
 569 tectonic deformation patterns. Therefore, in central Mongolia such fluid-domains should  
 570 form extended tubes aligned with tectonic block motion, compatible with what is observed  
 571 (e.g. Calais et al. 2003). It is currently unknown how these low-resistivity tube-like features  
 572 change northwards across the Bolnay fault zone and eastwards outside the Hangai block.

### 573 *5.2.3 Upper crustal structure*

574 **5.2.3.1 Fault zones and terrane sutures** In general, the upper crust below the Hangai  
 575 Dome is highly resistive ( $2000 - 20000 \Omega\text{m}$ , HB in Figs 18 and 19). This can be explained by  
 576 a pre-Cambrian, cratonic basement (Cunningham 2001). To the south in the VL, the near-

577 surface layer ( $< 1$  km) has a highly variable resistivity ( $10 - 2000 \Omega\text{m}$ ) This is consistent  
578 with porous sediments in an internal drainage basin between the Hangai and Altai mountains  
579 (Cunningham 2001; Ganbat & Demberel 2010).

580 In the resistivity model, several anomalous low-resistivity upper crustal features are  
581 imaged. To the south of the edge of the Hangai Dome a strong crustal conductor ( $20-$   
582  $100 \Omega\text{m}$ ; SHF in Fig. 23) is imaged in several disconnected fragments trending roughly  
583 east-west. This conductive feature was previously identified by Comeau et al. (2018c). It  
584 extends towards the mid-crust and appears to connect with the SHC at depth.

585 Segments of the SHF system (Cunningham 2001; Walker et al. 2007), which marks a  
586 terrane boundary (Badarch et al. 2002) and may be an ancient suture zone created during  
587 the closure of the Mongol-Okhotsk ocean (Van der Voo et al. 2015), are congruent with many  
588 of these anomalies. Fault zones are often regions of fractured, weakened crust that may have  
589 circulating fluids, which increase their conductivity (Unsworth & Bedrosian 2004). Thus,  
590 this could offer a potential explanation for these conductive anomalies. What is more, the  
591 lower crustal conductive zone (discussed above in Sec. 5.2.2) terminates abruptly at this  
592 zone, indicating the importance of this location as a major crustal boundary.

593 To the north, the resistivity model shows low resistive anomalies ( $50-100 \Omega\text{m}$ ; BUF in  
594 Figs 19 and 22) at shallow depths ( $< 1$  km) that become moderately resistive ( $200-1000 \Omega\text{m}$ )  
595 to depths of approximately 10 km and do not connect to lower crustal low-resistivity zones.  
596 They are long, semi-continuous features that trend roughly east-west.

597 They appear to be coincident with the surface traces of the eastern segments of the  
598 Bulnay fault zone (Calais et al. 2003; Rizza et al. 2015, see Fig. 22). As above, conductive  
599 anomalies such as these can often be explained by fault zones. However, at mid-crustal  
600 depths a strong conductive feature is not imaged. One explanation for why an electrical  
601 signature could be absent from the lower reaches of a fault zone is that the fault is dry  
602 and locked, often the case for fault zones with large and infrequent ruptures (Unsworth &  
603 Bedrosian 2004), as is the case for the Bulnay fault zone (Rizza et al. 2015).

604 To the south, the model images a set of east-west trending anomalies (BF and GAF in

605 Figs 18 and 19). They have a low-resistivity (20–100  $\Omega\text{m}$ ) to depths of approximately 20 km,  
606 and are surrounded by otherwise highly resistive crust ( $> 1000 \Omega\text{m}$ ). In the southwest of  
607 the model there is an isolated low-resistivity anomaly (5–50  $\Omega\text{m}$ ; GAC in Figs 18 and 19)  
608 at a depth of 10–25 km.

609 At the northern edge of the Gobi-Altai mountains runs a large fault zone known as the  
610 Bogd fault that has been responsible for several large rupture events, including a moment  
611 magnitude of 8.1 in 1957 (Walker et al. 2007; Rizza et al. 2015). Furthermore, this fault  
612 zone represents a significant terrane boundary (Badarch et al. 2002). The Gobi-Altai fault  
613 zone runs along the south of the Gobi-Altai mountain plateau (Calais et al. 2003; Walker  
614 et al. 2007). The contrasting properties observed across this zone may reflect the rheological  
615 differences between accreted terranes of different origins (see Guy et al., 2015 and refer-  
616 ences therein; Comeau et al., 2019b). Again, the location of the low-resistivity anomalies is  
617 coincident with these fault zones, and they offer a potential explanation for these features.

618 **5.2.3.2 South Hangai mineral zones** Anomalous, strongly conductive features (10–  
619 40  $\Omega\text{m}$ ) stretch from the surface to the mid-crust near the South Hangai Fault zone (SHF;  
620 see Fig. 23). They are subvertical, dipping slightly southwards.

621 Near the SHF is the Bayankhongor Ophiolite Belt (green area in Fig. 23) and the  
622 Bayankhongor Metallogenic Belt, which is an economically significant ore zone that includes  
623 important sources of gold and copper (e.g. Buchan et al. 2001). Many of the conductive  
624 anomalies are coincident with known mineral deposits (Comeau et al. 2018b). Furthermore,  
625 mineralization zones commonly have conductive signatures from associated sulfide mineral-  
626 ogy and related metamorphic processes (e.g. Unsworth & Bedrosian 2004). Therefore, the  
627 anomalous conductors may be explained by zones of mineralization.

628 **5.2.3.3 Tariat and Chuluut volcanic zones** Anomalous moderately resistive features  
629 (300–1,300  $\Omega\text{m}$ ) are imaged within the homogeneous and highly resistive upper crust ( $>$   
630 2000  $\Omega\text{m}$ ; HB) below the Tariat and Chuluut regions (TV and CV, along P4; see Figs 19  
631 and 22). These anomalous features are vertically extended through the crust and sit above



632 a deeper ( $>70$  km) bulging conductor, described above in section 5.2.1. Similar features are  
633 seen in the eastern Hangai below Tsenkher geothermal area (TGT in Fig. 19).

634 These regions are well-known volcanic zones. In fact, central Mongolia contains many  
635 volcanic provinces related to intraplate, alkaline basaltic volcanism (Barry et al. 2003; Hunt  
636 et al. 2012; Ancuta et al. 2018, see Fig. 1 for locations). The Tariat region is the youngest  
637 volcanic zone in central Mongolia with eruptions as recently as 5,000 years ago (Barry et al.  
638 2003). The Chuluut region, located 100 km to the south, is one of the largest volcanic  
639 provinces in central Mongolia and has erupted lavas from 0.3–6 million years ago (Ancuta  
640 et al. 2018). Based on a geochemical analysis of the erupted lavas, (Ancuta et al. 2018)  
641 estimated samples in these regions were derived from 4% partial melting at a depth of  
642 90 km and Harris et al. (2010) predicted fast magma ascent directly from the mantle with  
643 no crustal magma storage.

644 The anomalous features are spatially associated with the surface expressions of volcanism  
645 (volcanic cones and calderas) and modern-day hydrothermal activity (hot springs), suggest-  
646 ing a relation (Comeau et al. 2018a, see Fig. 1). Geochemical evidence is inconsistent with  
647 crustal melt storage below the Hangai Dome (e.g. Harris et al. 2010). Therefore, one poten-  
648 tial explanation for these features may be hydrothermal alteration from ancient conduits of  
649 hot magma as it moved through the crust (e.g. Cashman & Sparks 2013), which would pro-  
650 duce a small, but detectable, signature in the magnetotelluric data (Comeau 2015; Comeau  
651 et al. 2016).

652 Below these volcanic regions there is evidence that indicates partial melt generation in a  
653 shallowing asthenosphere (see Sec. 5.2.1). Therefore, the Tariat and Chuluut volcanism can  
654 be potentially traced throughout the lithospheric column, from the upper crustal anomalous  
655 zones possibly representing the signature of ancient magma conduits coincident with surface  
656 calderas, to the deep conductive zone possibly related to a shallowing asthenosphere and a  
657 source zone of partial melt. Consequently, this is a nice test of our inversion strategy that  
658 was designed to bridge multiple spatial scales.

**6 CONCLUSION**

In this study we present the first 3-D resistivity model of the Hangai and Gobi-Altai region in Mongolia. The final electrical resistivity model successfully resolves features across multiple spatial scales, featuring small ( $< 3$  km) crustal resistivity structures along with large-scale regional resistivity variations ( $>100$  km) at the Lithosphere-Asthenosphere boundary within the same self-consistent model.

Magnetotelluric data were acquired over an area of  $650 \times 400$  km<sup>2</sup> in the Hangai and Gobi-Altai mountains in central Mongolia. A station layout was designed that combines 97 sites on a regularly spaced 50 km grid with 175 sites along profiles and in local areas of interest that have a denser spacing of 5 to 15 km. Efficient data acquisition was achieved by the use of telluric-only instruments and deriving telluric-magnetotelluric transfer functions for the profiles. The estimated transfer functions used for the inversion covered a period range from 0.1 to 20000 s.

Numerical modelling and inversion of MT data that encompass a wide period range and a non-uniform site distribution poses a computationally challenging problem that requires an approach that can account for the inherent multiscale nature of the data. The addition of topography adds further complications. The technical aspects were addressed by using a finite-element method (FEM) inversion algorithm based on non-conforming hexahedral meshes, which facilitates multi-scale model parametrizations and allowed the incorporation of local topography while keeping computational cost feasible. Furthermore, we developed a multi-stage inversion methodology, whereby additional sites, a wider period range, and a finer model discretization was included in subsequent stages.

For Stage I, a regional 1-D resistivity model was derived to act as an initial model for Stage II, the 3-D inversion with data from the coarse grid sites. The resulting model was then passed on to Stage III, where all sites with denser spacing were added, followed by Stage IV with an extended period range and a finer mesh. This approach decreased the risk of landing in a geologically implausible local minimum of the parameter space. As a result,

686 we obtained a resistivity model that accurately resolves small resistivity structures in the  
687 crust together with regional resistivity variations down to the asthenosphere.

688 This approach can further be extended to both larger and smaller scales. For example,  
689 the use of long period instruments on a coarser grid could extend the model resolution  
690 beyond the lithosphere-asthenosphere-boundary. Alternatively, a focused inversion, limited  
691 to a small subset of the region but using a finer grid and short period transfer functions,  
692 could act as a high resolution fifth stage and facilitate local studies of mineralized (Comeau  
693 et al. 2018b) and geothermal zones (Batmagnai et al. 2019).

694 The final 3-D resistivity model reveals a highly resistive (2000–20000  $\Omega\text{m}$ ) upper crust  
695 (0–20 km) in the Hangai region, which is consistent with a pre-Cambrian, cratonic basement.  
696 Furthermore, many conductive anomalies are imaged in the upper crust that are coincident  
697 with, and can potentially be explained by surface observables, such as faults zones, mineral  
698 zones, volcanic provinces, and geothermal areas. Thanks to the multiscale approach, some  
699 of these anomalies can be traced continuously to asthenospheric depths. In contrast to the  
700 resistive upper crust, the lower crust (30–50 km) consists of well-resolved low-resistivity zones  
701 (5–50  $\Omega\text{m}$ ), some of them in tube-like shapes. A possible explanation are fluid-rich domains  
702 that are trapped within the ductile lower crust. A large low-resistivity zone (30–100  $\Omega\text{m}$ )  
703 is imaged in the upper mantle, which features features two localized upward bulges below  
704 the Hangai Dome. This result is consistent with a non-uniform lithosphere-asthenosphere  
705 boundary that contains small upwellings, shallowing to a depth of only 70 km. However, the  
706 origin of such upwellings can not be constrained with the resistivity model alone. It provides  
707 crucial structural information from the shallow crust to the upper mantle, but more research  
708 is needed to constrain the geodynamic processes, which are the cause for the upwelling and  
709 ultimately for the intraplate volcanism and the Hangai Dome uplift.

## 710 **ACKNOWLEDGEMENT**

711 This project was financially supported by the SNF (grant No. 200021L\_162660/1) and the  
712 DFG (grant No. BE5149/6-1) under the DACH program. This work was supported by

713 the Swiss National Supercomputing Center (CSCS) under project ID s828. We thank the  
714 Geophysical Instrument Pool Potsdam (GIPP) and the Geothermal Energy and Geofluids  
715 group (Department of Earth Sciences, ETH Zürich) for providing instruments. We thank  
716 the field crew and our colleagues from the Mongolian Academy of Science for their support:  
717 Batbileg Tegshjargal, Bayrjarga Bizya, Dominic Harpering, Dorian Sörgel, Eldev-Ochir Bold,  
718 Friedemann Samrock, Gantsogt Sukhbaatar, Jörg Schmalzl, Nasan-Ochir Tumen, Neeraj  
719 Sudhir, Nomuun Narantsogt, Phillip Kotowski, Robin Mann, Sandra Grazioli, Sukhbaatar  
720 Usnikh, Tsagaansukh Halzaa, Tserendug Shoovdor, Zagdsuren Shatar and more. We also  
721 want to thank Colin Farquharson and one anonymous reviewer for their detailed comments,  
722 which helped improve the manuscript.

## 723 REFERENCES

- 724 Alzetta, G., Arndt, D., Bangerth, W., Boddu, V., Brands, B., Davydov, D., Gassmüller, R.,  
725 Heister, T., Heltai, L., Kormann, K., et al., 2018. The deal. II library, version 9.0, *Journal of*  
726 *Numerical Mathematics*, **26**(4), 173–183.
- 727 Ancuta, L. D., Zeitler, P. K., Idleman, B. D., & Jordan, B. T., 2018. Whole-rock  $^{40}\text{Ar}/^{39}\text{Ar}$   
728 geochronology, geochemistry, and stratigraphy of intraplate Cenozoic volcanic rocks, central  
729 Mongolia, *Bulletin*, **130**(7-8), 1397–1408.
- 730 Aster, R. C., Borchers, B., & Thurber, C. H., 2018. *Parameter estimation and inverse problems*,  
731 Elsevier.
- 732 Badarch, G., Cunningham, W. D., & Windley, B. F., 2002. A new terrane subdivision for Mon-  
733 golia: implications for the Phanerozoic crustal growth of Central Asia, *Journal of Asian Earth*  
734 *Sciences*, **21**(1), 87–110.
- 735 Bahr, K., 1991. Geological noise in magnetotelluric data: a classification of distortion types,  
736 *Physics of the Earth and Planetary Interiors*, **66**(1), 24 – 38.
- 737 Balay, S., Abhyankar, S., Adams, M. F., Brown, J., Brune, P., Buschelman, K., Dalcin, L., Dener,  
738 A., Eijkhout, V., Gropp, W. D., Kaushik, D., Knepley, M. G., May, D. A., McInnes, L. C., Mills,  
739 R. T., Munson, T., Rupp, K., Sanan, P., Smith, B. F., Zampini, S., Zhang, H., & Zhang, H., 2018.  
740 PETSc users manual, Tech. Rep. ANL-95/11 - Revision 3.10, Argonne National Laboratory.
- 741 Bao, X., Eaton, D. W., & Guest, B., 2014. Plateau uplift in western Canada caused by lithospheric  
742 delamination along a craton edge, *Nature Geoscience*, **7**(11), 830.
- 743 Barry, T., Saunders, A., Kempton, P., Windley, B., Pringle, M., Dorjnamjaa, D., & Saandar, S.,

2003. Petrogenesis of Cenozoic basalts from Mongolia: evidence for the role of asthenospheric versus metasomatized lithospheric mantle sources, *Journal of Petrology*, **44**(1), 55–91.
- Batmagnai, E., Samrock, F., Grayver, Alexander, V., Kuvshinov, A., Saar, Martin, O., Demberel, S., Tsegmed, B., Tserendug, S., Purevsuren, D., & Oyuntsetseg, D., 2019. Integrated geoscientific exploration for geothermal energy utilization in the Mongolian Hangai, in *EGU General Assembly Conference Abstracts*, Vienna, Austria.
- Berdichevsky, M., Vanyan, L., Kuznetsov, V., Levadny, V., Mandelbaum, M., Nechaeva, G., Okulesky, B., Shilovsky, P., & Shpak, I., 1980. Geoelectrical model of the Baikal region, *Physics of the Earth and Planetary Interiors*, **22**(1), 1 – 11.
- Bertrand, E., Caldwell, T., Hill, G., Wallin, E., Bennie, S., Cozens, N., Onacha, S., Ryan, G., Walter, C., Zaino, A., et al., 2012. Magnetotelluric imaging of upper-crustal convection plumes beneath the Taupo Volcanic Zone, New Zealand, *Geophysical Research Letters*, **39**(2).
- Bird, P., 1979. Continental delamination and the Colorado Plateau, *Journal of Geophysical Research: Solid Earth*, **84**(B13), 7561–7571.
- Booker, J. R., 2014. The magnetotelluric phase tensor: A critical review, *Surveys in Geophysics*, **35**(1), 7–40.
- Buchan, C., Cunningham, D., Windley, B. F., & Tomurhuu, D., 2001. Structural and lithological characteristics of the Bayankhongor Ophiolite Zone, Central Mongolia, *Journal of the Geological Society*, **158**(3), 445–460.
- Cagniard, L., 1953. Basic theory of the magneto-telluric method of geophysical prospecting, *Geophysics*, **18**(3), 605–635.
- Calais, E., Vergnolle, M., San’Kov, V., Likhnev, A., Miroshnitchenko, A., Amarjargal, S., & Déverchère, J., 2003. GPS measurements of crustal deformation in the Baikal-Mongolia area (1994–2002): Implications for current kinematics of Asia, *Journal of Geophysical Research: Solid Earth*, **108**(B10).
- Campanyà, J., Ledo, J., Queralt, P., Marcuello, A., & Jones, A. G., 2014. A new methodology to estimate magnetotelluric (MT) tensor relationships: Estimation of Local transfer-functions by Combining Interstation Transfer-functions (ELICIT), *Geophysical Journal International*, **198**(1), 484–494.
- Cashman, K. V. & Sparks, R. S. J., 2013. How volcanoes work: A 25 year perspective, *GSA bulletin*, **125**(5-6), 664–690.
- Chen, M., Niu, F., Liu, Q., & Tromp, J., 2015. Mantle-driven uplift of Hangai Dome: New seismic constraints from adjoint tomography, *Geophysical Research Letters*, **42**(17), 6967–6974.
- Cherevatova, M., Smirnov, M. Y., Korja, T., Pedersen, L. B., Ebbing, J., Gradmann, S., Becken, M., Group, M. W., et al., 2015. Electrical conductivity structure of north-west Fennoscandia

- 779 from three-dimensional inversion of magnetotelluric data, *Tectonophysics*, **653**, 20–32.
- 780 Comeau, M., 2015. *Electrical Resistivity Structure of the Altiplano-Puna Magma Body and Volcan*  
781 *Uturuncu from Magnetotelluric Data: University of Alberta*, Ph.D. thesis, PhD thesis published  
782 by The University of Alberta Education and Research Archive, 337 pp.
- 783 Comeau, M. J., Unsworth, M. J., & Cordell, D., 2016. New constraints on the magma distri-  
784 bution and composition beneath Volcán Uturuncu and the southern Bolivian Altiplano from  
785 magnetotelluric data, *Geosphere*, **12**(5), 1391–1421.
- 786 Comeau, M. J., Becken, M., Käüfl, J., Kuvshinov, A., Demberel, S., & the Hangai Working Group,  
787 2018a. Images of intraplate volcanism: The upper crustal structure below Tariat volcanic zone,  
788 Mongolia, imaged with magnetotellurics, in *EGU General Assembly Conference Abstracts*, Vi-  
789 enna, Austria.
- 790 Comeau, M. J., Käüfl, J., Becken, M., Kuvshinov, A., Grayver, A., Kamm, J., Demberel, S.,  
791 Batmagnai, E., Tserendug, S., Eldev-Ochir, B., & Nasan-Ochir, T., 2018b. Electrical resistivity  
792 models reveal mineralization and fault systems in the Valley of the Lakes, south-central Mongolia,  
793 in *24th EM Induction Workshop Abstracts*, Helsingør, Denmark.
- 794 Comeau, M. J., Käüfl, J. S., Becken, M., Kuvshinov, A., Grayver, A. V., Kamm, J., Demberel, S.,  
795 Sukhbaatar, U., & Batmagnai, E., 2018c. Evidence for fluid and melt generation in response to  
796 an asthenospheric upwelling beneath the Hangai Dome, Mongolia, *Earth and Planetary Science*  
797 *Letters*, **487**, 201 – 209.
- 798 Comeau, M. J., Becken, M., Grayver, A., Käüfl, J., & Kuvshinov, A., 2019a. Can a conceptual  
799 mechanism of fluid focusing explain lower crustal conductors?, in *Schmucker-Weidelt Colloquium*  
800 *for Electromagnetic Depth Research*, Haltern am See, Germany.
- 801 Comeau, M. J., Becken, M., Käüfl, J., Grayver, A., Kuvshinov, A., Tserendug, S., Batmagnai,  
802 E., & Demberel, S., 2019b. Evidence for terrane boundaries and suture zones across Southern  
803 Mongolia detected with a 2-dimensional magnetotelluric transect, *Earth, Planets and Space*, in  
804 revision.
- 805 Connolly, J. & Podladchikov, Y. Y., 2013. A hydromechanical model for lower crustal fluid flow,  
806 in *Metasomatism and the chemical transformation of rock*, pp. 599–658, Springer.
- 807 Connolly, J. A. D. & Podladchikov, Y. Y., 2004. Fluid flow in compressive tectonic settings: Im-  
808 plications for midcrustal seismic reflectors and downward fluid migration, *Journal of Geophysical*  
809 *Research: Solid Earth*, **109**(B4).
- 810 Cunningham, W., 2001. Cenozoic normal faulting and regional doming in the southern Hangay  
811 region, Central Mongolia: implications for the origin of the Baikal rift province, *Tectonophysics*,  
812 **331**(4), 389–411.
- 813 Dmitriev, V. I., Il'inskii, A. S., & Sveshnikov, A. G., 1976. The developments of mathematical

- 814 methods for the study of direct and inverse problems in electrodynamics, *Russian Mathematical*  
815 *Surveys*, **31**(6), 133.
- 816 Dong, H., Wei, W., Jin, S., Ye, G., Zhang, L., Jing, J., Yin, Y., Xie, C., & Jones, A. G., 2016.  
817 Extensional extrusion: Insights into south-eastward expansion of Tibetan Plateau from magne-  
818 totelluric array data, *Earth and Planetary Science Letters*, **454**, 78 – 85.
- 819 Egbert, G. D., 2002. Processing and interpretation of electromagnetic induction array data,  
820 *Surveys in geophysics*, **23**(2-3), 207–249.
- 821 Egbert, G. D. & Booker, J. R., 1986. Robust estimation of geomagnetic transfer functions,  
822 *Geophysical Journal of the Royal Astronomical Society*, **87**(1), 173–194.
- 823 Ganbat, E. & Demberel, O., 2010. Geologic background of the Hangay geothermal system, west-  
824 central Mongolia, in *Proceedings World Geothermal Congress*, p. 1e6.
- 825 García, X. & Jones, A. G., 2005. A new methodology for the acquisition and processing of  
826 audio-magnetotelluric (AMT) data in the AMT dead band, *Geophysics*, **70**(5), G119–G126.
- 827 Grayver, A. V., 2015. Parallel three-dimensional magnetotelluric inversion using adaptive finite-  
828 element method. Part I: theory and synthetic study, *Geophysical Journal International*, **202**(1),  
829 584–603.
- 830 Grayver, A. V. & Kolev, T. V., 2015. Large-scale 3D geoelectromagnetic modeling using parallel  
831 adaptive high-order finite element method, *Geophysics*, **80**(6), E277–E291.
- 832 Grayver, A. V. & Kuvshinov, A. V., 2016. Exploring equivalence domain in nonlinear inverse  
833 problems using covariance matrix adaption evolution strategy (CMAES) and random sampling,  
834 *Geophysical Journal International*, **205**(2), 971–987.
- 835 Groom, R. W. & Bailey, R. C., 1989. Decomposition of magnetotelluric impedance tensors in the  
836 presence of local three-dimensional galvanic distortion, *Journal of Geophysical Research: Solid*  
837 *Earth*, **94**(B2), 1913–1925.
- 838 Guy, A., Schulmann, K., Janoušek, V., Štípská, P., Armstrong, R., Belousova, E., Dolgoplova,  
839 A., Seltmann, R., Lexa, O., Jiang, Y., et al., 2015. Geophysical and geochemical nature of  
840 relaminated arc-derived lower crust underneath oceanic domain in southern Mongolia, *Tectonics*,  
841 **34**(5), 1030–1053.
- 842 Harpering, D., 2018. *Robust processing scheme for magnetotelluric data*, Master’s thesis, WWU  
843 Münster.
- 844 Harris, N., Hunt, A., Parkinson, I., Tindle, A., Yondon, M., & Hammond, S., 2010. Tectonic im-  
845 plications of garnet-bearing mantle xenoliths exhumed by Quaternary magmatism in the Hangay  
846 dome, central Mongolia, *Contributions to Mineralogy and Petrology*, **160**(1), 67–81.
- 847 Heise, W., Bibby, H. M., Caldwell, T. G., Bannister, S. C., Ogawa, Y., Takakura, S., & Uchida,  
848 T., 2007. Melt distribution beneath a young continental rift: the Taupo Volcanic Zone, New

- 849 Zealand, *Geophysical Research Letters*, **34**(14).
- 850 Hermance, J. F. & Thayer, R. E., 1975. The telluric-magnetotelluric method, *Geophysics*, **40**(4),  
851 664–668.
- 852 Hill, G. J., Bibby, H. M., Ogawa, Y., Wallin, E. L., Bennie, S. L., Caldwell, T. G., Keys, H.,  
853 Bertrand, E. A., & Heise, W., 2015. Structure of the Tongariro Volcanic system: Insights from  
854 magnetotelluric imaging, *Earth and Planetary Science Letters*, **432**, 115–125.
- 855 Hunt, A. C., Parkinson, I., Harris, N., Barry, T., Rogers, N., & Yondon, M., 2012. Cenozoic vol-  
856 canism on the Hangai Dome, Central Mongolia: geochemical evidence for changing melt sources  
857 and implications for mechanisms of melting, *Journal of Petrology*, **53**(9), 1913–1942.
- 858 Illiceto, V. & Santarato, G., 1986. On the possibility of the telluric method: some results on faulted  
859 structures, *Geophysical prospecting*, **34**(7), 1082–1098.
- 860 Ionov, D., 2002. Mantle structure and rifting processes in the Baikal–Mongolia region: geophysical  
861 data and evidence from xenoliths in volcanic rocks, *Tectonophysics*, **351**(1-2), 41–60.
- 862 Joshi, A., Bangerth, W., & Seveck-Muraca, E. M., 2004. Adaptive finite element based tomography  
863 for fluorescence optical imaging in tissue, *Optics Express*, **12**(22), 5402–5417.
- 864 Karypis, G. & Kumar, V., 1999. A fast and highly quality multilevel scheme for partitioning  
865 irregular graphs, *Journal on Scientific Computing*, **20**(1), 359–392.
- 866 Käüfl, J. S., Grayver, A. V., & Kuvshinov, A. V., 2018. Topographic distortions of magnetotelluric  
867 transfer functions: a high-resolution 3-d modelling study using real elevation data, *Geophysical*  
868 *Journal International*, **215**(3), 1943–1961.
- 869 Kay, R. W. & Kay, S. M., 1993. Delamination and delamination magmatism, *Tectonophysics*,  
870 **219**(1-3), 177–189.
- 871 Khoza, T. D., Jones, A. G., Muller, M. R., Evans, R. L., Miensopust, M. P., & Webb, S. J., 2013.  
872 Lithospheric structure of an Archean craton and adjacent mobile belt revealed from 2-D and 3-D  
873 inversion of magnetotelluric data: Example from southern Congo craton in northern Namibia,  
874 *Journal of Geophysical Research: Solid Earth*, **118**(8), 4378–4397.
- 875 Krystopowicz, N. J. & Currie, C. A., 2013. Crustal eclogitization and lithosphere delamination  
876 in orogens, *Earth and Planetary Science Letters*, **361**, 195–207.
- 877 Liu, L. & Hasterok, D., 2016. High-resolution lithosphere viscosity and dynamics revealed by  
878 magnetotelluric imaging, *Science*, **353**(6307), 1515–1519.
- 879 Manning, C. E., 2018. Fluids of the lower crust: deep is different, *Annual Review of Earth and*  
880 *Planetary Sciences*, **46**, 67–97.
- 881 McDannell, K. T., Zeitler, P. K., & Idleman, B. D., 2018. Relict topography within the Hangay  
882 Mountains in central Mongolia: Quantifying long-term exhumation and relief change in an old  
883 landscape, *Tectonics*, **37**(8), 2531–2558.



- 884 Meissner, R. & Mooney, W., 1998. Weakness of the lower continental crust: a condition for  
885 delamination, uplift, and escape, *Tectonophysics*, **296**(1-2), 47–60.
- 886 Melosh, G., Cumming, W., Benoit, D., Wilmarth, M., Colvin, A., Winick, J., Soto-Neira, E.,  
887 Sussman, D., Urzúa-Monsalve, L., Powell, T., et al., 2010. Exploration results and resource  
888 conceptual model of the Tolhuaca geothermal field, Chile, in *Proceedings, World Geothermal*  
889 *Congress*.
- 890 Meqbel, N. M., Egbert, G. D., Wannamaker, P. E., Kelbert, A., & Schultz, A., 2014. Deep  
891 electrical resistivity structure of the northwestern US derived from 3-D inversion of USArray  
892 magnetotelluric data, *Earth and Planetary Science Letters*, **402**, 290–304.
- 893 Miensoopust, M. P., 2017. Application of 3-D electromagnetic inversion in practice: Challenges,  
894 pitfalls and solution approaches, *Surveys in Geophysics*, **38**(5), 869–933.
- 895 Muñoz, G., 2014. Exploring for geothermal resources with electromagnetic methods, *Surveys in*  
896 *geophysics*, **35**(1), 101–122.
- 897 Murphy, B. S. & Egbert, G. D., 2017. Electrical conductivity structure of southeastern North  
898 America: implications for lithospheric architecture and Appalachian topographic rejuvenation,  
899 *Earth and Planetary Science Letters*, **462**, 66–75.
- 900 NASA JPL, 2013. NASA Shuttle Radar Topography Mission Global 1 arc second. NASA LP  
901 DAAC, <https://doi.org/10.5067/MEaSUREs/SRTM/SRTMGL1.003>.
- 902 Nieuwenhuis, G., Unsworth, M. J., Pana, D., Craven, J., & Bertrand, E., 2014. Three-dimensional  
903 resistivity structure of Southern Alberta, Canada: implications for Precambrian tectonics, *Geo-*  
904 *physical Journal International*, **197**(2), 838–859.
- 905 Oyuntsetseg, D., Ganchimeg, D., Minjigmaa, A., Ueda, A., & Kusakabe, M., 2015. Isotopic and  
906 chemical studies of hot and cold springs in western part of Khangai Mountain region, Mongolia,  
907 for geothermal exploration, *Geothermics*, **53**, 488–497.
- 908 Peacock, J. R., Mangan, M. T., McPhee, D., & Wannamaker, P. E., 2016. Three-dimensional  
909 electrical resistivity model of the hydrothermal system in Long Valley Caldera, California, from  
910 magnetotellurics, *Geophysical Research Letters*, **43**(15), 7953–7962.
- 911 Petit, C., Tiberi, C., Deschamps, A., & Déverchère, J., 2008. Teleseismic traveltimes, topography  
912 and the lithospheric structure across central Mongolia, *Geophysical Research Letters*, **35**(11).
- 913 Platz, A. & Weckmann, U., 2019. An automated new pre-selection tool for noisy Magnetotel-  
914 luric data using the Mahalanobis distance and magnetic field constraints, *Geophysical Journal*  
915 *International*.
- 916 Priestley, K., Debayle, E., McKenzie, D., & Pilidou, S., 2006. Upper mantle structure of eastern  
917 Asia from multimode surface waveform tomography, *Journal of Geophysical Research: Solid*  
918 *Earth*, **111**(B10).

- 919 Rikitake, T., 1948. Notes on electromagnetic induction within the Earth, *Bull. Earthq. Res. Inst.*,  
920 **24**(1), 4.
- 921 Rizza, M., Ritz, J.-F., Prentice, C., Vassallo, R., Braucher, R., Larroque, C., Arzhannikova, A.,  
922 Arzhannikov, S., Mahan, S., Massault, M., et al., 2015. Earthquake geology of the Bulnay fault  
923 (Mongolia), *Bulletin of the Seismological Society of America*, **105**(1), 72–93.
- 924 Robertson, K., Heinson, G., & Thiel, S., 2016. Lithospheric reworking at the Proterozoic-  
925 Phanerozoic transition of Australia imaged using AusLAMP Magnetotelluric data, *Earth and*  
926 *Planetary Science Letters*, **452**, 27 – 35.
- 927 Robertson, K., Heinson, G., Taylor, D., & Thiel, S., 2017. The lithospheric transition between  
928 the Delamerian and Lachlan orogens in western Victoria: new insights from 3D magnetotelluric  
929 imaging, *Australian Journal of Earth Sciences*, **64**(3), 385–399.
- 930 Rousseeuw, P. J., 1984. Least median of squares regression, *Journal of the American Statistical*  
931 *Association*, **79**(388), 871–880.
- 932 Rung-Arunwan, T., Siripunvaraporn, W., & Utada, H., 2016. On the Berdichevsky average,  
933 *Physics of the Earth and Planetary Interiors*, **253**, 1 – 4.
- 934 Sahagian, D., Proussevitch, A., Ancuta, L., Idleman, B., & Zeitler, P., 2016. Uplift of Central  
935 Mongolia recorded in vesicular basalts, *The Journal of Geology*, **124**(4), 435–445.
- 936 Samrock, F., Grayver, A. V., Eysteinnsson, H., & Saar, M. O., 2018. Magnetotelluric image of  
937 transcrustal magmatic system beneath the Tulu Moye geothermal prospect in the Ethiopian rift,  
938 *Geophysical Research Letters*, **45**(23), 12–847.
- 939 Sheldrick, T. C., Barry, T. L., Millar, I. L., Barfod, D. N., Halton, A. M., & Smith, D. J.,  
940 2019. Evidence for southward subduction of the mongol-okhotsk oceanic plate: implications  
941 from mesozoic adakitic lavas from mongolia, *Gondwana Research*.
- 942 Smith, J. T., 1997. Estimating galvanic-distortion magnetic fields in magnetotellurics, *Geophysical*  
943 *Journal International*, **130**(1), 65–72.
- 944 Styron, R., 2018. GEM global active faults, <http://doi.org/10.5281/zenodo.1404388>.
- 945 Tiberi, C., Deschamps, A., Déverchère, J., Petit, C., Perrot, J., Appriou, D., Mordvinova, V.,  
946 Dugaarma, T., Ulzibaat, M., & Artemiev, A., 2008. Asthenospheric imprints on the lithosphere in  
947 central Mongolia and southern Siberia from a joint inversion of gravity and seismology (MOBAL  
948 experiment), *Geophysical Journal International*, **175**(3), 1283–1297.
- 949 Tietze, K. & Ritter, O., 2013. Three-dimensional magnetotelluric inversion in practice-the electri-  
950 cal conductivity structure of the San Andreas Fault in Central California, *Geophysical Journal*  
951 *International*, **195**(1), 130–147.
- 952 Tikhonov, A., 1950. On determining electrical characteristics of the deep layers of the Earths  
953 crust, in *Doklady*, vol. 73, pp. 295–297, Citeseer.

- 954 Tikhonov, A. N., 1963. On the solution of ill-posed problems and the method of regularization,  
955 in *Doklady Akademii Nauk*, vol. 151, pp. 501–504, Russian Academy of Sciences.
- 956 Unsworth, M. & Bedrosian, P. A., 2004. Electrical resistivity structure at the SAFOD site from  
957 magnetotelluric exploration, *Geophysical Research Letters*, **31**(12).
- 958 Unsworth, M. & Rondenay, S., 2013. *Mapping the Distribution of Fluids in the Crust and Litho-*  
959 *spheric Mantle Utilizing Geophysical Methods*, pp. 535–598, Springer Berlin Heidelberg, Berlin,  
960 Heidelberg.
- 961 Usui, Y., Ogawa, Y., Aizawa, K., Kanda, W., Hashimoto, T., Koyama, T., Yamaya, Y., &  
962 Kagiya, T., 2016. Three-dimensional resistivity structure of Asama volcano revealed by data-  
963 space magnetotelluric inversion using unstructured tetrahedral elements, *Geophysical Journal*  
964 *International*, **208**(3), 1359–1372.
- 965 Van der Voo, R., van Hinsbergen, D. J., Domeier, M., Spakman, W., & Torsvik, T. H., 2015.  
966 Latest Jurassic–earliest Cretaceous closure of the Mongol-Okhotsk Ocean: A paleomagnetic and  
967 seismological-tomographic analysis, *Geological Society of America Special Papers*, **513**, 589–606.
- 968 Vergnolle, M., Pollitz, F., & Calais, E., 2003. Constraints on the viscosity of the continental crust  
969 and mantle from GPS measurements and postseismic deformation models in western Mongolia,  
970 *Journal of Geophysical Research: Solid Earth*, **108**(B10).
- 971 Walker, R., Nissen, E., Molor, E., & Bayasgalan, A., 2007. Reinterpretation of the active faulting  
972 in central Mongolia, *Geology*, **35**(8), 759–762.
- 973 Walker, R., Molor, E., Fox, M., & Bayasgalan, A., 2008. Active tectonics of an apparently aseis-  
974 mic region: distributed active strike-slip faulting in the Hangay Mountains of central Mongolia,  
975 *Geophysical Journal International*, **174**(3), 1121–1137.
- 976 Weidelt, P., 1972. The inverse problem of geomagnetic induction, *J. Geophys.*, **38**, 257–289.
- 977 Windley, B. F. & Allen, M. B., 1993. Mongolian plateau: Evidence for a late Cenozoic mantle  
978 plume under central Asia, *Geology*, **21**(4), 295–298.
- 979 Xu, S., Unsworth, M. J., Hu, X., & Mooney, W. D., 2019. Magnetotelluric evidence for asym-  
980 metric simple shear extension and lithospheric thinning in south China, *Journal of Geophysical*  
981 *Research: Solid Earth*, **124**(1), 104–124.
- 982 Yang, B., Egbert, G. D., Kelbert, A., & Meqbel, N. M., 2015. Three-dimensional electrical  
983 resistivity of the north-central USA from EarthScope long period magnetotelluric data, *Earth*  
984 *and Planetary Science Letters*, **422**, 87 – 93.
- 985 Yungul, S. H., 1977. The telluric methods in the study of sedimentary structures-a survey, *Geo-*  
986 *exploration*, **15**(4), 207–238.
- 987 Zhang, F., Wu, Q., Grand, S. P., Li, Y., Gao, M., Demberel, S., Ulziibat, M., & Sukhbaatar, U.,  
988 2017. Seismic velocity variations beneath central Mongolia: Evidence for upper mantle plumes?,

